Scientia Iranica A (2019) 26(4), 2057–2078

Sharif University of Technology
Scientia Iranica
Transactions A: Civil Engineering
http://scientiairanica.sharif.edu

Invited Paper

Analysis of laminated composite plates based on THB-RKPM method using the higher-order shear deformation plate theory

H.R. Atri and S. Shojaee*

Department of Civil Engineering, Shahid Bahonar University of Kerman, Kerman, Iran.

Received 26 November 2018; received in revised form 26 February 2019; accepted 13 May 2019

KEYWORDS
Laminated composite plates;
Higher-order shear deformation theory;
NURBS;
THB-splines;
Reproducing kernel particle method

Abstract. In the present investigation, static free vibration and buckling response of laminated composite plates based on coupling of Truncated Hierarchical B-splines (THB-splines) with Reproducing Kernel Particle Method (RKPM) through higher-order shear deformation plate theory are presented. The coupled THB-RKPM method blends the advantages of the isogeometric analysis and meshfree methods. Since under certain conditions, the isogeometric B-spline and NURBS basis functions are exactly represented by reproducing kernel meshfree shape functions, recursive process of producing isogeometric bases can be omitted. More importantly, a seamless link between meshfree methods and isogeometric analysis can easily be defined, which provides an authentic meshfree approach to refining the model locally in isogeometric analysis. This procedure can be carried out using truncated hierarchical B-splines to construct new bases and adaptively refine them. It is shown that the THB-RKPM method is ideally appropriate for local refinement of laminated composite plates in the framework of isogeometric analysis. The flexibility of the proposed method for refining basis functions leads to decrease in the computational cost without losing the accuracy of the solution. Numerical examples considering different boundary conditions and various aspect ratios, stiffness ratios, and fiber orientations demonstrated validity and versatility of the proposed method.

1. Introduction

In recent years, increase in the use of conventional and unconventional multilayered structures has led to major improvements in aerospace, automotive, and ship vehicles. Owing to the high strength to weight and stiffness to weight ratios, composite structures have attracted great attention of researchers and engineers [1,2]. Besides possessing superior composite material properties, laminated composites provide convenient design through tailoring of the stacking sequence and layer thickness to optimize the desired characteristics for engineering applications, e.g., some of the structures such as sandwich panels, which consist of 3 layers, are a special case of laminated composite structures with large difference between material properties of core and face sheets [3] or layered ceramic-metallic structures, which are employed as thermal protection, have been used for over three decades [4]. On the other hand, new unconventional materials, such as piezoelectric ones, which are used in Functionally Graded Materials (FGMs) [5,6], and the so-called smart structures [7] are characterized by continuously varying

*. *Corresponding author. Fax: +98 3433220054*
E-mail address: saeed.shojaee@uk.ac.ir (S. Shojaee)

doi: 10.24200/sci.2019.21417

mechanical and/or thermal properties. In fact, smart structures, which are distinguished from conventional ones by the presence of integrated actuator, sensor, and controller elements, involve interactions between mechanical and electric fields. They are also designed to actively react to disturbance forces and maintain or even improve the level of performance.

As far as multilayered structures are widely used in practice, studying the bending and free vibration as well as buckling analysis of laminated composite structures is an indispensable task in many applications. Moreover, the advent of new materials and the use of multilayered configurations have led to a significant increase in the modelling of plates and shells. To date, various methods have been proposed by a number of researchers concentrating on the analysis of laminated composite plates and shells, e.g., Carrera et al. considered refined finite elements solutions for anisotropic laminated plates [8] and Reddy studied linear and nonlinear finite element analyses of laminated plates and shells [9]. Due to the limitations of finite element methods in the exact modeling of geometries, the so-called isogeometric analysis (IGA) has been proposed by Hughes et al. [10] with the aim of integrating the Finite Element Analysis (FEA) into the conventional NURBS-based Computer Aided Design (CAD) tools. In addition to representing exact geometries, CAD basis functions (e.g., NURBS) can provide any order of continuity through a simple procedure. Hence, many researchers have exploited the higher-order continuity of isogeometric formulation in the analysis of laminated plates and shells, e.g., a model for laminated composite plates and shells based on the finite cell method in the framework of isogeometric analysis was proposed by Guo and Ruess [11]. Recently, a formulation based on NURBS basis functions to study the global response of cross-ply laminated composites was investigated by Natarajan et al. [12], which suffered from shear locking. Due to the use of lower-order NURBS basis functions, they proposed an artificial shear correction factor that was problem dependent. In addition, Thai et al. [13] developed a NURBS-based isogeometric approach associated with the layerwise deformation theory for analysis of laminated composites and sandwich plate structures. In another study by Thai et al. [14], an isogeometric formulation based on third-order shear deformation theory was presented for static free vibration and buckling analysis of laminated composite plate structures. However, CAD basis functions possess important properties, which are required in numerical analysis, but suffer from the rigidity of classical tensor-product construction. During the last decades, considerable attention has been given to circumventing the tensor-product constructions, which are expressed in terms of B-spline representation. These constructions hinder the possibility of accommodating trimmed surfaces, adaptive local refinement, or incongruent surface descriptions at opposing faces. Several different schemes have been developed to provide more flexible solutions that support localized refinement. Some of the relevant issues are addressed in T-splines [15], hierarchical B-splines [16], PHT-splines [17], locally refined splines [18], and truncated hierarchical B-splines [19]. T-splines are defined by control meshes that allow the introduction of the so-called T-junctions. Since the initial definition of T-splines did not guarantee linear independence [20], analysis-suitable T-splines [21] were subsequently introduced to provide this property. However, local refinement in analysis-suitable T-splines may go beyond the domain of interest. PHT-spline–a polynomial spline over hierarchical T-meshes–was introduced for stitching several surface patches [17]. The basis functions of PHT-splines have the main properties of B-splines, such as non-negativity, local support, and partition of unity. They also have the same important properties as those of T-splines, like adaptivity. In contrast to T-splines, which are rational, PHT-splines are polynomial and they are only C^1-continuous, which can be mentioned as their main drawback. Locally Refined Splines (LR-Splines) are based on splitting the tensor-product of basis functions, which leads to challenges with the linear independence [18] that was solved in [22]. Local refinement strategies for adaptive isogeometric analysis using LR B-splines are proposed in [23].

Hierarchical B-splines were first introduced by Forsey and Bartels [16] and have further been elaborated on in [24]. The classical hierarchical B-splines suffer from linear independence property, which has been solved by Kraft [24]. A major drawback of standard hierarchical B-splines is their weakness in providing the partition of unity property. In order to alleviate this disadvantage, a truncated mechanism was developed in [19]. As reported in [19], the truncated basis for hierarchical splines ensures partition of unity, linear independence, and local refinability. Since THB-splines possess the convex hull property, they are appropriate for geometric modeling and surface reconstructions; thus, they can be used in computer aided design. Additionally, THB-splines are suitable for adaptive numerical solutions; therefore, they can be utilized as an effective approach to isogeometric analysis.

On the other hand, many efforts have been made to blend IGA and meshfree methods in order to open a pathway for taking advantage of the strengths of both techniques. The so-called meshless or meshfree methods have been focused on overcoming the difficulties associated with structured nodal connectivity. However, most of the meshless methods [25] are based on an approximation of field variables and do not satisfy Kronecker delta property [26]. Some researchers have paid great attention to blending advantageous techniques of meshfree approximants and isogeometric analysis, e.g., in [27], Local Maximum Entropy (LME) approximation was coupled with isogeometric analysis. This coupling strategy exploited the best features and overcame the main drawbacks of each of these approximants [27]. In fact, the IGA method preserved veracity representation of problem domain boundary and meshfree methods dealt with unstructured grids and the possible local refinement. In another research, Valizadeh et al. [28] proposed a methodology based on the coupling of isogeometric analysis with Reproducing Kernel Particle Method (RKPM), which was a representative of a class of meshfree methods. The domain interior was discretized by RKPM, while IGA provided geometrically exact model discretization. Another meshless method, namely Natural Element Method (NEM), developed by Sambridge et al. [29], endowed advantageous properties of both meshless and finite element methods [26]. In a research by Gonzalez et al. [30], it was shown that NEM was equivalent to isogeometric analysis. However, this method did not rely on an underlying tensor-product quadrilateral mesh [30]. Zhang and Wang [31] introduced a consistently coupled isogeometric-meshfree method based on the reproducing conditions. In order to achieve a consistently coupled approximation, a mixed reproducing point vector was proposed to ensure arbitrary order monomial reproducibility for isogeometric basis functions and reproducing kernel meshfree shape functions. Chi et al. [32] presented a meshfree analysis framework whereby the NURBS boundary surface was provided by CAD tools to describe the exact geometry of the problem and the flexibility of meshfree approximants was used to enhance the solution accuracy. Although isogeometric meshfree coupled methods combine the benefit of geometry exactness of IGA with adaptivity of meshfree approximations, the basis functions in these coupled methods are different. To circumvent this drawback, Zhang and Wang [31] recently introduced a reproducing kernel meshfree formulation for isogeometric basis functions. It was shown that by properly introducing meshfree nodes, support size, and consistency conditions, the reproducing kernel meshfree shape functions could exactly recover B-spline and NURBS basis functions. Moreover, the proposed formulation offered a meshfree strategy for the local model refinement in isogeometric analysis.

The present paper is based on the new concept of THB-RKPM method, which was established in [33], to investigate the capability of hierarchical bases with truncation and reproducing kernel particle method in bending, free vibration, and buckling analysis of laminated composite plate structures by means of showing numerical results for well-known benchmark examples. In the proposed method, the meshfree construction of B-spline or NURBS basis functions is carried out through a one-step approach instead of using recursive process. Then, truncation mechanism is used to provide local model refinement. First, the initial shape or basis functions are defined by knot vectors. Then, the corresponding meshfree nodes are obtained according to the reproducing kernel formulation. Thereafter, instead of inserting additional knots into the initial knot vectors, adaptive refinement using truncated hierarchical splines is used to compute the new linear reproducing points. Thus, the local refinement is achieved by adding new meshfree nodes to the originally left nodes. It turns out that a seamless link between meshfree methods and truncated hierarchical B-splines can conveniently be defined.

The paper is arranged as follows: the basic definitions of B-splines, THB-splines, RKPM basis functions, and the coupled THB-RKPM method are provided in Section 2. The isogeometric formulation of laminated composite plates using THB-RKPM based on HSDT is presented in Section 3. Section 4 gives various numerical examples to illustrate local refinement performance using the coupled isogeometric-meshfree method in comparison with the NURBS uniform refinement case. Concluding remarks are provided in Section 5.

2. Isogeometric fundamentals in summary

In this section, a brief description of B-splines and NURBS is given. At first, some basic definitions of knot vectors as well as B-spline basis functions, curves, and surfaces are provided. Then, the hierarchical and truncated hierarchical B-splines are introduced. The reproducing kernel particle method and its relation with isogeometrics are also discussed here.

2.1. Definition and basic properties

A knot vector given as $\Xi = \{\xi_1, \xi_2, \cdots, \xi_{n+p+1}\}$ is a non-decreasing sequence of parameter values, where ξ_i represents the ith knot, n is the number of basis functions, and p is the polynomial degree. When the first and last knots of a knot vector have multiplicity $p+1$, the vector is known as *open*. Univariate B-spline basis functions are defined recursively using Cox-de Boor formula [34]:

$$N_{i,0}(\xi) = \begin{cases} 1 & \text{if } \xi_i \le \xi \le \xi_{i+1} \\ 0 & \text{otherwise} \end{cases} \tag{1}$$

and for $p \ge 1$:

$$N_{i,p}(\xi) = \frac{\xi - \xi_i}{\xi_{i+p} - \xi_i} N_{i,p-1}(\xi) + \frac{\xi_{i+p+1} - \xi}{\xi_{i+p+1} - \xi_{i+1}} N_{i+1,p-1}(\xi). \tag{2}$$

A basis function of degree p spans up to $p+1$ elements and the basis functions constructed by open knot

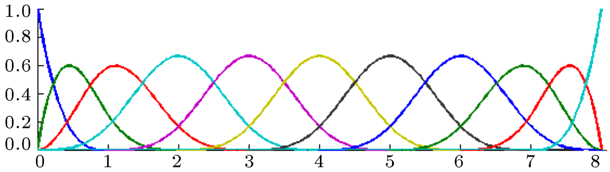

Figure 1. Cubic B-splines basis functions.

vectors are interpolatory at the boundaries. Moreover, they possess important properties such as partition of unity, non-negativity, and linear independence. An example of cubic basis functions with an open knot vector is shown in Figure 1.

The reproducing conditions for B-spline basis functions can be defined as follows [32]:

$$\sum_{i=1}^{n} N_{i,p}(\xi)\mathbf{p}\left(\xi_i^{[\cdot]}\right) = \mathbf{p}(\xi), \tag{3}$$

where $\mathbf{p}(\xi)$ is a monomial basis vector given as:

$$\mathbf{p}(\xi) = \left\{1, \xi, \eta, \xi^2, \xi\eta, \eta^2, \cdots, \xi^p, \cdots, \eta^p\right\}^T, \tag{4}$$

and $\mathbf{p}\left(\xi_i^{[\cdot]}\right)$ is defined as:

$$\mathbf{p}\left(\xi_i^{[\cdot]}\right) = \left\{1, \xi_i^{[1]}, \left(\xi_i^{[2]}\right)^2, \cdots, \left(\xi_i^{[p]}\right)^p\right\}^T, \tag{5}$$

in which $\xi_i^{[l]}$ is the reproducing point for the monomial ξ^l. By defining an operator $S_p^l[G]$, the reproducing point $\xi_i^{[l]}$ can be expressed as:

$$\xi_i^{[l]} = \sqrt[l]{\frac{S_p^l\left[G_{i+1}^{i+p}\right]}{C_p^l}}, \qquad C_p^l = \frac{p!}{l!(p-l)!}. \tag{6}$$

If needed, refer to [32] for more details on the operator $S_p^l[G]$ and reproducing points of B-spline basis functions.

A piecewise polynomial B-spline curve is given by the linear combination of control points $\mathbf{P}_i$ and the respective basis functions $N_{i,p}(\xi)$:

$$\mathbf{C}(\xi) = \sum_{i=1}^{n} N_{i,p}(\xi)\mathbf{P}_i. \tag{7}$$

A B-spline surface is computed by the Cartesian product of B-spline basis functions $N_{i,p}(\xi)$ and $M_{j,q}(\eta)$ in two parametric dimensions ξ and η:

$$\mathbf{S}(\xi,\eta) = \sum_{i=1}^{n}\sum_{j=1}^{m} N_{i,p}(\xi)M_{j,q}(\eta)\mathbf{P}_{i,j}. \tag{8}$$

The generalization of B-splines, called NURBS, has the ability to exactly represent all quadric surfaces, such as cylinders, spheres, ellipsoids, etc. NURBS are rational functions of B-splines and, similar to B-spline ones, NURBS-based curves and surfaces are defined as:

$$\mathbf{C}(\xi) = \frac{\sum_{i=1}^{n} N_{i,p}(\xi)w_i\mathbf{P}_i}{\sum_{j=1}^{n} N_{j,p}(\xi)w_j}, \tag{9}$$

$$\mathbf{S}(\xi,\eta) = \frac{\sum_{i=1}^{n}\sum_{j=1}^{m} N_{i,p}(\xi)M_{j,q}(\eta)w_{i,j}}{\sum_{k=1}^{n}\sum_{l=1}^{m} N_{k,p}(\xi)M_{l,q}(\eta)w_{i,j}}\mathbf{P}_{i,j}, \tag{10}$$

where w_i is a set of positive weights, which allows NURBS to exactly represent conic sections.

2.2. Hierarchical B-splines

Given a knot vector $\boldsymbol{\Xi} = \{\xi_1, \xi_2, \cdots, \xi_{n+p+1}\}$, the B-spline basis functions, $N_{i,p}(\xi)$, with a local support on $[\xi_i, \xi_{i+p+1}]$ are refinable, which allows construction of hierarchical B-splines. Suppose $N_{i,p}^{\ell}$ represents basis functions with the parametric domain Ω^ℓ defined on the knot vector $\boldsymbol{\Xi}^\ell$ at the level ℓ ($\ell = 0, 1, \cdots$). B-spline basis functions, $N_{i,p}^{\ell+1}$, associated with level $\ell+1$ are obtained by bisecting the knot vector of the previous level ℓ. The basis functions defined on the refined knot sequence, $\boldsymbol{\Xi}^{\ell+1}$, are the children of $N_{i,p}^{\ell}$ defined on $\boldsymbol{\Xi}^\ell$. Therefore, a basis function $N_{i,p}^{\ell}$ on the level ℓ can be represented as a linear combination of $p+2$ of its children as follows:

$$N_{i,p}^{\ell}(\xi) = \sum_{r=0}^{p+1} \alpha_r^p N_{2i+r,p}^{\ell+1}(\xi) \qquad \text{with}$$

$$\alpha_r^p = \frac{1}{2^p}\binom{p+1}{r}, \tag{11}$$

where $N_{2i+r,p}^{\ell+1}(\xi)$ represents the children of $N_{i,p}^{\ell}$ and α_r^p represents the binomial coefficients. For bivariate basis functions, the procedure is the same; given two knot vectors $\boldsymbol{\Xi}$ and $\mathbf{H}$, a bivariate B-spline basis $\mathbf{N_{i,p}(\boldsymbol{\xi},\boldsymbol{\eta})}$ with local support $[\xi_i, \xi_{i+p+1}] \times [\eta_j, \eta_{j+q+1}]$ has $(p+2)\times(q+2)$ children, in which p and q are polynomial degrees of basis functions. The process of hierarchical refinement, replacing coarse grid bases with fine B-spline ones, is as follows: Suppose $\mathcal{N}^\ell$ is the tensor product of B-spline basis functions at level ℓ with parametric domain Ω^ℓ. Then, find a set of basis functions $\mathfrak{N} \in \mathcal{N}^\ell$ in such way that supp $\mathfrak{N} \not\subset \Omega^{\ell+1}$. Next, identify the children of $\mathfrak{N}$ at level $\ell+1$ so that $\mathfrak{N} \in \mathcal{N}^{\ell+1}$ and supp $\mathfrak{N} \subseteq \Omega^{\ell+1}$. Finally, gather all the active basis functions at levels ℓ and $\ell+1$ as follows:

$$\mathcal{H} = \left\{\mathfrak{N} \in \mathcal{N}^\ell : \text{supp } \mathfrak{N} \not\subset \Omega^{\ell+1}\right\}$$
$$\cup \left\{\mathfrak{N} \in \mathcal{N}^{\ell+1} : \text{supp } \mathfrak{N} \subseteq \Omega^{\ell+1}\right\}$$
$$\text{for} \quad \ell = 0, \cdots, \ell_{\max} - 1. \tag{12}$$

Eq. (12) defines the recursive construction of hierarchical B-splines. However, hierarchical bases are globally linearly independent [24], but they do not ensure partition of unity, which leads to overlapping of basis functions that may produce bad numerical conditioning. To overcome the deficiencies of hierarchical B-splines, the truncated operation is presented [19].

2.3. Truncated hierarchical B-splines

The truncation mechanism for hierarchical B-splines basis was first introduced by Giannelli et al. [19]. Truncated hierarchical B-splines satisfy partition of unity, reduce support overlapping, and preserve the geometry. Since they are natural extensions of classical B-splines, they have similar properties such as partition of unity, convex hull, non-negativity, and compact support. Very similar to hierarchical B-splines, truncated bases can be constructed only by truncating the basis functions $\mathfrak{N} \in \mathcal{N}^{\ell}$ with supp $\mathfrak{N} \not\subset \Omega^{\ell+1}$. This mechanism is using Eq. (11) and defining a basis function $\mathbf{t} \subseteq \Omega^{\ell}$ with respect to the finer basis of $\mathfrak{N} \in \mathcal{N}^{\ell+1}$, as follows:

$$\mathbf{t} = \sum_{\mathfrak{N} \in \mathcal{N}^{\ell+1}} \alpha_{\mathfrak{N}}^{\ell+1} \mathfrak{N}, \qquad \alpha_{\mathfrak{N}}^{\ell+1} \in \mathbb{R}. \tag{13}$$

The truncated basis function of $\mathbf{t}$ with respect to $\mathcal{N}^{\ell+1}$ can be expressed as:

$$\mathrm{trunc}^{\ell+1}\mathbf{t} = \sum_{\mathfrak{N} \in \mathcal{N}^{\ell+1}, \mathrm{supp}\ \mathfrak{N} \not\subset \Omega^{\ell+1}} \alpha_{\mathfrak{N}}^{\ell+1} \mathfrak{N},$$

$$\alpha_{\mathfrak{N}}^{\ell+1} \in \mathbb{R}. \tag{14}$$

According to Eq. (14), the truncation of a basis function is to discard active children whose support has a non-empty overlap with $\Omega^{\ell+1}$. It should be noted that the truncation of a function is applied in terms of basis functions of the finer hierarchical levels through a recursive procedure. Figure 2 illustrates the construction process of hierarchical and truncated hierarchical B-splines for two levels, namely 0 and 1, of B-spline basis functions. The level-0 basis functions, which are shown in blue curves, are defined on the cubic knot vector $\Xi^0 = \{0, 1, \cdots, 8\}$, whereas green curves represent level-1 basis functions obtained by subdivision of Ξ^0. Let the blue dashed curve with the black area domain Ω^1 in Figure 2(a) be such a basis function to be refined. In terms of refinability, the level-0 blue dashed basis function can be replaced by its 5 children defined at level 1, as shown in green solid curves in Figure 2(b). All level-1 basis functions whose support is not in Ω^1 are depicted as dashed curves and known as passive basis. The remaining solid curves are known as active and, by taking the union of all solid curves from levels 0 and 1, the hierarchical B-spline bases of level 1 can be obtained; see Figure 2(c). As can be seen in the construction process of hierarchical basis, there are too many overlaps of basis functions at different levels, which leads to weakness in providing the partition of unity property. To resolve this issue, among the 4 basis functions adjacent to the blue dashed curve, those with active level-1 basis functions should be truncated. Each of the blue solid curves has 5 children; each child with supports fully contained in Ω^1 should be discarded and the remaining active children are collected to form the truncated hierarchical B-splines; see Figure 2(d). Similarly, the truncation mechanism can be implemented for bivariate basis functions. Figure 3 shows an example of bivariate B-spline and truncated hierarchical B-spline basis functions for the procedure presented in Figure 2.

2.4. RKPM basis functions

The parametric domain Ω_{ξ}, which is discretized by a set of particles, ξ_k ($k = 1, \cdots, np$), is employed in this study to present meshfree shape functions. The association between a particle, ξ_k, and a field point, ξ, is defined by the kernel function $\Upsilon(\xi_k - \xi)$. The influence domain of kernel function is often

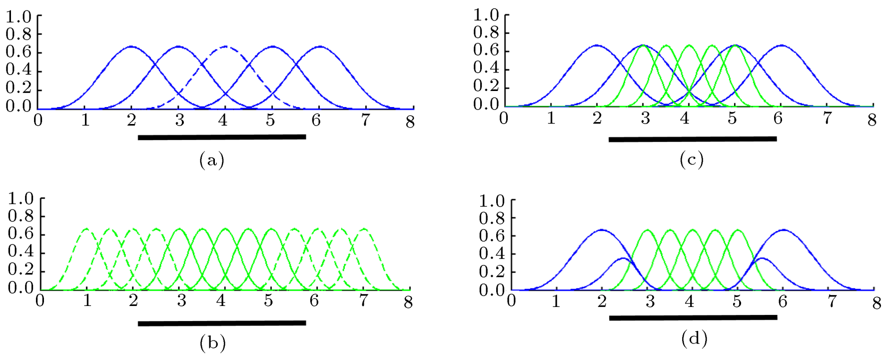

Figure 2. The procedure to construct univariate cubic HB- and THB-splines: (a) The blue dashed curve represents a to-be-refined basis function known as passive, (b) the green solid curves represent active level-1 basis functions, (c) the combination of active basis functions from the previous two levels to construct the hierarchical B-splines, and (d) five children of each solid curve with supports fully contained in the black area are discarded and the remaining active basis functions are collected to construct THB-splines.

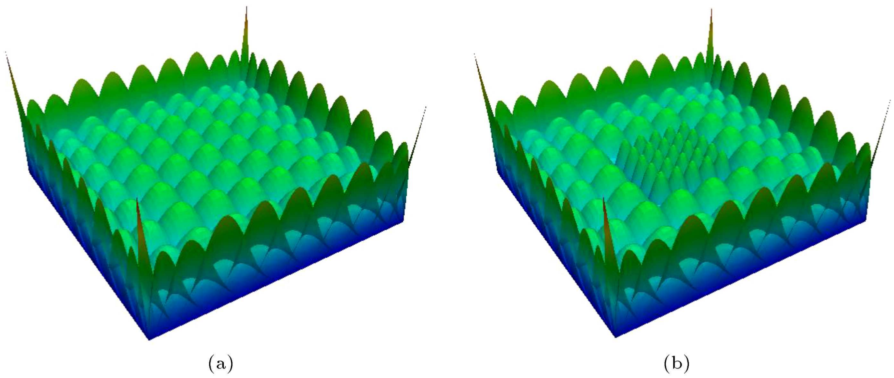

Figure 3. Truncation mechanism for bivariate basis functions: (a) Uniform B-spline basis functions and (b) truncated hierarchical B-spline basis functions.

expressed as supp (ξ_k) measured by z. The union of nodal supports covers the parametric domain Ω_ξ. By imposing the polynomial reproducing condition, the discrete Reproducing Kernel (RK) can be defined as:

$$u^h(\xi) = \sum_{k=1}^{np} \Phi(\xi) d_k, \tag{15}$$

where d_k is a coefficient associated with node k and $\Phi(\xi)$ is the meshfree shape function that can be expressed as [35]:

$$\Phi_k(\xi) = \mathbf{p}^T(\xi)\mathbf{a}(\xi)\Upsilon(\xi_k - \xi), \tag{16}$$

where $\mathbf{p}(\xi)$ is defined according to Eq. (4) and $\mathbf{a}(\xi)$ is an unknown coefficient vector that can be obtained by enforcing the pth order reproducing conditions as follows:

$$\sum_{k=1}^{np} \Phi_k(\xi)\xi_k^i \eta_k^j = \xi^i \eta^j, \qquad 0 \le i + j \le p. \tag{17}$$

Eq. (17) can be rewritten in a vector form with the aid of Eq. (4):

$$\sum_{k=1}^{np} \Phi_k(\xi)\mathbf{p}(\xi_k) = \mathbf{p}(\xi). \tag{18}$$

Substituting Eq. (16) into Eq. (18) yields:

$$\mathbf{M}(\xi)\mathbf{a}(\xi) = \mathbf{p}(\xi), \tag{19}$$

where $\mathbf{M}(\xi)$ is the moment matrix:

$$\mathbf{M}(\xi) = \sum_{k=1}^{np} \mathbf{p}^T(\xi_k)\mathbf{p}(\xi_k)\Upsilon(\xi_k - \xi). \tag{20}$$

With the aid of Eq. (19), the meshfree shape function $\Phi_k(\xi)$ can be obtained as:

$$\Phi_k(\xi) = \mathbf{p}^T(\xi_k)\mathbf{M}^{-1}(\xi)\mathbf{p}(\xi)\Upsilon(\xi_k - \xi). \tag{21}$$

2.5. Meshfree local refinement based on THB-splines

As discussed in [31], after properly introducing meshfree nodes, support size, and consistency conditions, the reproducing kernel meshfree shape functions are capable of exactly representing the isogeometric B-spline and NURBS basis functions. This correspondence provides a great tool for local model refinement, and node insertion can readily be realized in isogeometric analysis. In order to make great flexibility regarding adaptive local refinement of IGA basis functions, this technique is coupled with truncated hierarchical B-splines; see [33]. For the sake of brevity, the local refinement procedure is discussed for one-dimensional basis functions. The readers who are interested in the 2D case can refer to [33] for more details.

In the 1D case, let us consider initial basis functions defined by the following knot vector:

$$\xi = \{0, 0, 0, 1, 2, 3, 4, 5, 6, 6, 6\}. \tag{22}$$

The corresponding meshfree nodes are obtained according to Eq. (6) as:

$$\xi^{[1]} = \left\{0, \frac{1}{2}, \frac{3}{2}, \frac{5}{2}, \frac{7}{2}, \frac{9}{2}, \frac{11}{2}, 6\right\}. \tag{23}$$

The initial basis functions with the aid of reproducing kernel meshfree formulation are shown in Figure 4. The corresponding meshfree nodes are denoted by green circles.

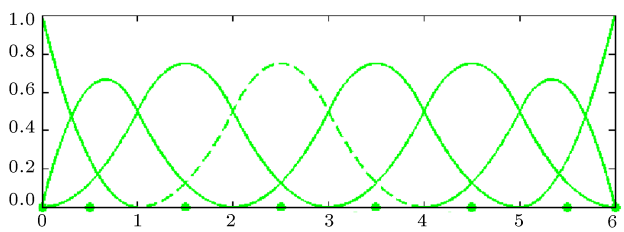

Figure 4. Initial basis functions with corresponding meshfree nodes before local refinement.

Now, suppose the domain $\Omega_\xi^e = [2,3]$ is the area to be refined. First, the related basis function spans in the domain are designated by the green dashed curve. According to Eq. (11), this basis function can be represented by its children. Among the children, those with supports fully contained in Ω_ξ^e should be discarded and the remaining children are considered as active. By collecting all the active basis functions, the truncated hierarchical B-splines can be constructed. The related meshfree nodes based on truncation mechanism are:

$$\xi^{[1]} = \left\{0, \frac{1}{2}, \frac{3}{2}, \frac{19}{8}, \frac{5}{2}, \frac{21}{8}, \frac{7}{2}, \frac{9}{2}, \frac{11}{2}, 6\right\}. \tag{24}$$

The local model refinement in a preferable meshfree environment with the new corresponding meshfree nodes (blue and red circles) is depicted in Figure 5. It should be noted that the meshfree node from the previous level is kept and the new nodes are added into the domain. In comparison with [31], re-computing the shape functions based on the new node group is omitted, since the original basis functions are truncated to produce the new basis ones. This means that, instead of calculating all basis functions, only a number of bases are modified and new meshfree nodes are produced. For fine levels of refinement, one can see [33]. The construction process of meshfree nodes is illustrated in Algorithm 1, where the step associated with truncation mechanism is discussed in Section 2.3.

It should be noticed that the new meshfree nodes are constructed through the truncation mechanism; they are interpreted as the field variables and the values of solution field are defined in these nodes.

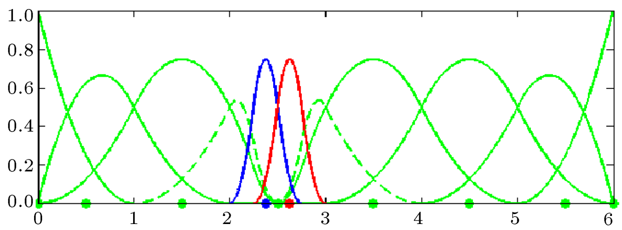

Figure 5. Refined basis functions with the corresponding meshfree nodes after local refinement.

```
Input: Knot vector
Calculate meshfree nodes from Eq. (6)
Construct basis functions from Eq. (21)
For every span to be refined do
    For every level of refinement do
        Perform truncation mechanism
        Calculate new meshfree nodes
    End for
End for
Output: Truncated basis and meshfree nodes
```

Algorithm 1. THB-RKPM refinement.

3. An isogeometric formulation for laminated composite plates using THB-RKPM based on HSDT model

3.1. Reddy's third-order shear deformation plate theory

A higher-order shear deformation plate theory has been developed by Reddy [36] in which the transverse shear strains are assumed to be parabolically distributed across the thickness. The displacement components are defined as:

$$U(x,y,z) = u_0(x,y) + z\theta_y(x,y) + cz^3\left[\frac{\partial w_0(x,y)}{\partial x} + \theta_y(x,y)\right],$$

$$c = \frac{-4}{3h^2}, \tag{25a}$$

$$V(x,y,z) = v_0(x,y) - z\theta_x(x,y) + cz^3\left[\frac{\partial w_0(x,y)}{\partial y} - \theta_x(x,y)\right], \tag{25b}$$

$$W(x,y,z) = w_0(x,y), \tag{25c}$$

where u_0, v_0, and w_0 denote the displacements of an arbitrary point in the plate, and θ_x and θ_y are the rotations of the normal to the mid-plane about the x and y axes, respectively. The in-plane strain vector, $\{\varepsilon\}$, and transverse shear strain vector, $\{\gamma\}$, have the following forms; $(,)$ indicates the partial derivative:

$$\{\varepsilon\} = \begin{Bmatrix} \varepsilon_x \\ \varepsilon_y \\ \gamma_{xy} \end{Bmatrix} = \begin{Bmatrix} u_{0,x} \\ v_{0,y} \\ u_{0,y} + v_{0,x} \end{Bmatrix} + z\begin{Bmatrix} \theta_{y,x} \\ -\theta_{x,y} \\ \theta_{y,y} - \theta_{x,x} \end{Bmatrix} + cz^3\begin{Bmatrix} w_{0,xx} + \theta_{y,x} \\ w_{0,yy} - \theta_{x,y} \\ 2w_{0,xy} + \theta_{y,x} - \theta_{x,x} \end{Bmatrix}, \tag{26a}$$

$$\{\gamma\} = \begin{Bmatrix} \gamma_{xz} \\ \gamma_{yz} \end{Bmatrix} = \begin{Bmatrix} \theta_y + w_{0,x} \\ -\theta_x + w_{0,y} \end{Bmatrix} + 3cz^2\begin{Bmatrix} \theta_y + w_{0,x} \\ -\theta_x + w_{0,y} \end{Bmatrix}. \tag{26b}$$

Or the compact form is:

$$\{\varepsilon\} = \{\varepsilon_m\} + z\{\varepsilon_b\} + cz^3\{\varepsilon_p\}, \tag{27a}$$

$$\{\gamma\} = \{\gamma_s\} + 3cz^2\{\gamma_{sw}\}, \tag{27b}$$

where ε_m, ε_b, and ε_p denote membrane linear strain, bending strain, and warping strain, respectively; also, γ_s and γ_{sw} indicate the first-order transverse shear strain and shear-warp strain, respectively. The stress-strain relations of an orthotropic layer in the local coordinate system can be expressed as:

$$\begin{Bmatrix} \sigma_1 \\ \sigma_2 \\ \tau_{12} \\ \tau_{13} \\ \tau_{23} \end{Bmatrix} = \begin{bmatrix} Q_{11} & Q_{12} & 0 & 0 & 0 \\ Q_{21} & Q_{22} & 0 & 0 & 0 \\ 0 & 0 & Q_{66} & 0 & 0 \\ 0 & 0 & 0 & Q_{44} & 0 \\ 0 & 0 & 0 & 0 & Q_{55} \end{bmatrix} \times \begin{Bmatrix} \varepsilon_1 \\ \varepsilon_2 \\ \gamma_{12} \\ \gamma_{13} \\ \gamma_{23} \end{Bmatrix}, \tag{28}$$

where the constants are given as:

$$Q_{11} = \frac{E_1}{1 - \upsilon_{12}\upsilon_{21}}, \qquad Q_{12} = \frac{\upsilon_{12}E_2}{1 - \upsilon_{12}\upsilon_{21}},$$

$$Q_{22} = \frac{E_2}{1 - \upsilon_{12}\upsilon_{21}},$$

$$Q_{66} = G_{12}, \qquad Q_{44} = G_{13}, \qquad Q_{55} = G_{23}. \tag{29}$$

In the above equation, E_1 and E_2 are Young's moduli parallel to and perpendicular to the fibers orientation, respectively; G_{12}, G_{23}, and G_{13} are the shear moduli; and υ_{12} and υ_{21} are the Poisson's ratios.

Since the laminate is usually made of several orthotropic layers the material coordinate system of which is oriented arbitrarily with respect to the laminate axes, the constitutive equation of each layer must be transformed to the laminate coordinates (x, y, z). The constitutive equation which relates the stresses to the strains in the laminate coordinates can be stated as:

$$\begin{Bmatrix} \sigma_x \\ \sigma_y \\ \tau_{xy} \\ \tau_{xz} \\ \tau_{yz} \end{Bmatrix} = \begin{bmatrix} \bar{Q}_{11} & \bar{Q}_{12} & \bar{Q}_{16} & 0 & 0 \\ \bar{Q}_{21} & \bar{Q}_{22} & \bar{Q}_{26} & 0 & 0 \\ \bar{Q}_{61} & \bar{Q}_{62} & \bar{Q}_{66} & 0 & 0 \\ 0 & 0 & 0 & \bar{Q}_{44} & \bar{Q}_{45} \\ 0 & 0 & 0 & \bar{Q}_{54} & \bar{Q}_{55} \end{bmatrix} \times \begin{Bmatrix} \varepsilon_x \\ \varepsilon_y \\ \gamma_{xy} \\ \gamma_{xz} \\ \gamma_{yz} \end{Bmatrix}, \tag{30}$$

where $\bar{Q}_{ij}$ $(i, j = 1, 2, 4, 5, 6)$ represents the transformed reduced stiffness coefficients of the plate [9]. The stress resultants and couples are defined by:

$$\begin{bmatrix} N_x & M_x & P_x \\ N_y & M_y & P_y \\ N_{xy} & M_{xy} & P_{xy} \end{bmatrix} = \int_{-\frac{h}{2}}^{\frac{h}{2}} \begin{Bmatrix} \sigma_x \\ \sigma_y \\ \tau_{xy} \end{Bmatrix} (1, z, z^3) dz, \tag{31a}$$

$$\begin{bmatrix} Q_x & R_x \\ Q_y & R_y \end{bmatrix} = \int_{-\frac{h}{2}}^{\frac{h}{2}} \begin{Bmatrix} \tau_{xz} \\ \tau_{yz} \end{Bmatrix} (1, z^2) dz, \tag{31b}$$

where N and Q are the membrane and transverse shear forces, respectively; M is bending moment per unit length; and P and R are the higher-order bending moment and shear forces, respectively. By substituting Eq. (28) into Eq. (31), the stress resultants are related to the strains as follows:

$$\begin{bmatrix} \bar{N} \\ \bar{M} \\ \bar{P} \end{bmatrix} = \begin{bmatrix} A & B & E \\ B & D & F \\ E & F & H \end{bmatrix} \begin{Bmatrix} \varepsilon_m \\ \varepsilon_b \\ \varepsilon_p \end{Bmatrix}, \tag{32a}$$

$$\begin{bmatrix} \bar{Q} \\ \bar{R} \end{bmatrix} = \begin{bmatrix} A^s & D^s \\ D^s & F^s \end{bmatrix} \begin{Bmatrix} \gamma_s \\ \gamma_{sw} \end{Bmatrix}, \tag{32b}$$

where A_{ij}, B_{ij}, etc. are the plate stiffnesses defined by:

$$(A_{ij}, B_{ij}, D_{ij}, E_{ij}, F_{ij}, H_{ij}) = \sum_{k=1}^{N} \int_{z_k}^{z_{k+1}} \bar{Q}_{ij}^{(k)} (1, z, z^2, z^3, z^4, z^6) dz, \tag{33a}$$

$$\left(A_{ij}^s, D_{ij}^s, F_{ij}^s\right) = \sum_{k=1}^{N} \int_{z_k}^{z_{k+1}} \bar{Q}_{ij}^{(k)} (1, z^2, z^4) dz. \tag{33b}$$

The stiffnesses in Eq. (33a) are defined for $(i, j = 1, 2, 6)$ and other stiffness coefficients in Eq. (33b) are defined for $(i, j = 4, 5)$.

3.2. Governing equations

The governing equations of the higher-order theory will be derived according to Hamilton's variational principle:

$$\int_{t_1}^{t_2} \delta(U - W - T) dt = 0, \tag{34a}$$

$$U = U_1 + U_2, \tag{34b}$$

in which the virtual strain energy, δU_1, the potential energy subjected to in-plane mechanical loads, δU_2, the virtual work done by the applied external forces, δW, and the virtual kinetic energy, δT, are given by:

$$\delta U_1 = \int_{t_1}^{t_2} \left\{ \frac{1}{2} \delta \int \sigma_{ij} \varepsilon_{ij} dv \right\} dt, \tag{35}$$

$$\delta U_2 = \int_{t_1}^{t_2} \left\{ \frac{1}{2} \delta \int \sigma_{ij}^0 u_{s,i} . u_{s,j} dv \right\} dt, \tag{36}$$

$$\delta T = \int_{t_1}^{t_2} \left\{ \frac{1}{2} \delta \int \{\dot{u}\}^T \rho \{\dot{u}\} dv \right\} dt, \tag{37}$$

$$\delta W = \int_{t_1}^{t_2} \left\{ \int F . \delta u dv \right\} dt. \tag{38}$$

In the above equations, σ_{ij} and ε_{ij} are stress and strain components, respectively; ρ is the density of the plate material; σ_{ij}^0 denotes the initial stress components due to in-plane mechanical loads; and u_s is displacement components (U, V, W). Using THB-RKPM method, the variables at the control points, also called control variables, are the in-plane extensions, transverse deflection, and the rotations in a vector form as follows:

$$d = \{u_0, v_0, w_0, \theta_x, \theta_y\}. \tag{39}$$

The solution field is approximated as:

$$u=\sum_{k=1}^{n\times m}\mathrm{trunc}^{\ell}\mathbf{t}_k d_k, \tag{40}$$

where $\mathrm{trunc}^{\ell}\mathbf{t}_k$ is the coupled THB-RKPM basis of the level ℓ and $n\times m$ is the number of control points. By substituting Eq. (40) into Eq. (27), the relationship between strains and displacements can be expressed as:

$$\begin{bmatrix}\varepsilon_m & \varepsilon_b & \varepsilon_p & \gamma_s & \gamma_{sw}\end{bmatrix}^T=\sum_{k=1}^{n\times m}\begin{bmatrix}B_k^m & B_k^b & B_k^p & B_k^s & B_k^{sw}\end{bmatrix} d_k. \tag{41}$$

The strain-displacement matrices are written as:

$$[B_k^m]=\begin{bmatrix}R_{k,x} & 0 & 0 & 0 & 0\\ 0 & R_{k,y} & 0 & 0 & 0\\ R_{k,y} & R_{k,x} & 0 & 0 & 0\end{bmatrix}, \tag{42a}$$

$$[B_k^b]=\begin{bmatrix}0 & 0 & 0 & R_{k,x} & 0\\ 0 & 0 & 0 & 0 & R_{k,y}\\ 0 & 0 & 0 & R_{k,y} & R_{k,x}\end{bmatrix}, \tag{42b}$$

$$[B_k^p]=c\begin{bmatrix}0 & 0 & R_{k,xx} & R_{k,x} & 0\\ 0 & 0 & R_{k,yy} & 0 & R_{k,y}\\ 0 & 0 & 2R_{k,xy} & R_{k,y} & R_{k,x}\end{bmatrix}, \tag{42c}$$

$$[B_k^s]=\begin{bmatrix}0 & 0 & R_{k,x} & R_k & 0\\ 0 & 0 & R_{k,y} & 0 & R_k\end{bmatrix}, \tag{42d}$$

$$[B_k^{sw}]=3c\begin{bmatrix}0 & 0 & R_{k,x} & R_k & 0\\ 0 & 0 & R_{k,y} & 0 & R_k\end{bmatrix}. \tag{42e}$$

From Eqs. (27) and (31), δU_1 can be obtained as:

$$\delta U_1=\frac{1}{2}\delta\int_{\Omega}\Big([\varepsilon_m]^T[N]+[\varepsilon_b]^T[M]+[\varepsilon_p]^T[P]+[\gamma_s]^T[Q]+[\gamma_{sw}]^T[R]\Big)d\Omega. \tag{43}$$

By using Eq. (32) in Eq. (43) and applying the strain-displacement matrices, δU_1 can be rewritten as:

$$\delta U_1=\frac{1}{2}\delta\{d\}^T([K])\{d\}, \tag{44}$$

where $[K]$ is the linear stiffness matrix and can be calculated as follows:

$$\begin{aligned}[K]=&\int_{\Omega}\Big([B_m]^T[A][B_m]+[B_m]^T[B][B_b]+[B_m]^T[E][B_p]\Big)d\Omega+\int_{\Omega}\Big([B_b]^T[B][B_m]\\&+[B_b]^T[D][B_b]+[B_b]^T[F][B_p]\Big)d\Omega+\int_{\Omega}\Big([B_p]^T[E][B_m]+[B_p]^T[F][B_b]\\&+[B_p]^T[H][B_p]\Big)d\Omega+\int_{\Omega}\Big([B_s]^T[A^s][B_s]+[B_s]^T[D^s][B_{sw}]+[B_{sw}]^T[D^s][B_s]\\&+[B_{sw}]^T[F^s][B_{sw}]\Big)d\Omega.\end{aligned} \tag{45}$$

With respect to displacement components (U,V,W), Eq. (36) can be obtained as:

$$\begin{aligned}\delta U_2=&\frac{1}{2}\delta\int_{V}\big[\sigma_x^0\left(U_x^2+V_x^2+W_x^2\right)+\sigma_y^0\left(U_y^2+V_y^2+W_y^2\right)\\&+2\tau_{xy}^0\left(U_xU_y+V_xV_y+W_xW_y\right)\\&+2\tau_{xz}^0(U_xU_z+V_xV_z)+2\tau_{yz}^0(U_yU_z+V_yV_z)\big]\,dV.\end{aligned} \tag{46}$$

Like Eq. (35), Eq. (46) can be expressed in expanded form as:

$$\delta U_2=\frac{1}{2}\delta\{d\}^T[K_G]\{d\}, \tag{47}$$

where:

$$[K_G]=\int_{\Omega}[G]^T[\tau][G]d\Omega, \tag{48}$$

in which $[K_G]$ is the geometric stiffness matrix and other quantities are as follows:

$$[G]^T=\begin{bmatrix}R_{k,x} & R_{k,y} & 0 & 0 & 0 & 0 & 0 & 0 & 0 & 0\\ 0 & 0 & R_{k,x} & R_{k,y} & 0 & 0 & 0 & 0 & 0 & 0\\ 0 & 0 & 0 & 0 & R_{k,x} & R_{k,y} & 0 & 0 & 0 & 0\\ 0 & 0 & 0 & 0 & 0 & 0 & R_{k,x} & R_{k,y} & 0 & 0\\ 0 & 0 & 0 & 0 & 0 & 0 & 0 & 0 & R_{k,x} & R_{k,y}\end{bmatrix}, \tag{49}$$

$$[\boldsymbol{\tau}]=h\begin{bmatrix}\hat{\boldsymbol{\sigma}}_\mathbf{0} & \mathbf{0} & \mathbf{0} & \mathbf{0} & \mathbf{0}\\ \mathbf{0} & \hat{\boldsymbol{\sigma}}_\mathbf{0} & \mathbf{0} & \mathbf{0} & \mathbf{0}\\ \mathbf{0} & \mathbf{0} & \hat{\boldsymbol{\sigma}}_\mathbf{0} & \mathbf{0} & \mathbf{0}\\ \mathbf{0} & \mathbf{0} & \mathbf{0} & \hat{\boldsymbol{\sigma}}_\mathbf{0} & \mathbf{0}\\ \mathbf{0} & \mathbf{0} & \mathbf{0} & \mathbf{0} & \hat{\boldsymbol{\sigma}}_\mathbf{0}\end{bmatrix}, \tag{50}$$

where h is the thickness of the plate and $\hat{\boldsymbol{\sigma}}_\mathbf{0}$ is a matrix related to pre-buckling stresses:

$$\hat{\boldsymbol{\sigma}}_0 = \begin{bmatrix} \sigma_x^0 & \tau_{xy}^0 \\ \tau_{xy}^0 & \sigma_y^0 \end{bmatrix}. \tag{51}$$

For free vibration analysis of composite plates, Eq. (37) can be rewritten as:

$$\delta T = \frac{1}{2}\delta \int \rho \left(\dot{U}^2 + \dot{V}^2 + \dot{W}^2\right) dv. \tag{52}$$

With the aid of Eq. (40) and substituting Eq. (25a) into Eq. (52), the virtual kinetic energy can be obtained as:

$$\delta T = \frac{1}{2}\delta \left\{\dot{d}\right\}^T [M] \left\{\dot{d}\right\}, \tag{53}$$

where the global mass matrix $[M]$ is given as:

$$[M] = \int \left[\tilde{N}\right]^T [m] \left[\tilde{N}\right] d\Omega, \tag{54}$$

in which the details of $[\tilde{N}]^T = \{N_1 \quad N_2 \quad N_3\}$ and $[m]$ are as follows:

$$N_1 = \begin{bmatrix} R_k & 0 & 0 & 0 & 0 \\ 0 & 0 & 0 & R_k & 0 \\ 0 & 0 & R_{k,x} & R_k & 0 \end{bmatrix},$$

$$N_2 = \begin{bmatrix} 0 & R_k & 0 & 0 & 0 \\ 0 & 0 & 0 & 0 & R_k \\ 0 & 0 & R_{k,y} & 0 & R_k \end{bmatrix},$$

$$N_3 = \begin{bmatrix} 0 & 0 & R_k & 0 & 0 \\ 0 & 0 & 0 & 0 & 0 \\ 0 & 0 & 0 & 0 & 0 \end{bmatrix}, \tag{55}$$

$$[m] = \begin{bmatrix} \mathbf{I}_0 & 0 & 0 \\ 0 & \mathbf{I}_0 & 0 \\ 0 & 0 & \mathbf{I}_0 \end{bmatrix},$$

where:

$$\mathbf{I}_0 = \begin{bmatrix} I_1 & I_2 & cI_4 \\ I_2 & I_3 & cI_5 \\ cI_4 & cI_5 & c^2 I_7 \end{bmatrix},$$

$$(I_1, I_2, I_3, I_4, I_5, I_7) = \int_{-h/2}^{-h/2} \rho(1, z, z^2, z^3, z^4, z^6) dz. \tag{56}$$

From Eqs. (44), (47), and (53), and minimizing each term with respect to the generalized displacement vector $\{d\}$, the formulation of HSDT plate for static analysis is obtained as:

$$[K]\{d\} = \{F\}. \tag{57}$$

Free vibration equation is:

$$\left([K] - \omega^2 [M]\right)\{d\} = 0. \tag{58}$$

And buckling analysis can be stated as:

$$\left([K] + \lambda\left[K_G\right]\right)\{d\} = 0, \tag{59}$$

where ω and λ are natural frequency and critical buckling values, respectively. Since truncated hierarchical basis functions are a new class of B-splines, they are C^{p-1}-continuous and easily satisfy C^1-requirement in the approximate formulation of the HSDT model. It is worth mentioning that local refinement based on THB-RKPM decreases the computational cost without attenuating accuracy of the solution.

4. Numerical results

In this section, bending, free vibration, and buckling of laminated composite plates with rectangular and circular shapes using the coupling of truncated hierarchical B-splines with RKPM are studied. The results obtained by THB-RKPM are compared with other published data. For all numerical results, the elements integrated with $(p+1)(q+1)$ Gauss points are used. The material parameters are given as:

For isotropic plates:

- **Material I:** $E_1 = E_2 = 1$; $G_{12} = G_{13} = G_{23} = E_2/2(1+\nu)$; $\nu = 0.25$; $\rho = 1$.

For laminated plates:

- **Material II:** $E_1 = 25E_2$; $G_{12} = G_{13} = 0.5E_2$; $G_{23} = 0.2E_2$; $\nu_{12} = 0.25$; $\rho = 1$;
- **Material III:** $E_1/E_2 = 10, 20, 30, 40$; $G_{12} = G_{13} = 0.6E_2$; $G_{23} = 0.5E_2$; $\nu_{12} = 0.25$; $\rho = 1$;
- **Material IV:** $E_1 = 2.45E_2$; $G_{12} = G_{13} = 0.48E_2$; $G_{23} = 0.2E_2$; $\nu_{12} = 0.23$; $\rho = 1$.

Since THB-RKPM bases like NURBS basis functions are noninterpolatory, similar to many meshfree methods, the Kronecker delta properties are not satisfied. Therefore, several techniques have been developed to overcome the drawback [25]. If Dirichlet boundary condition is inhomogeneous, the Lagrange multiplier method [37] can be adopted. In our work, since the homogeneous Dirichlet boundary condition is used, zero values can easily and directly be imposed on control variables as in the standard finite element analysis.

4.1. Analysis of isotropic plates

4.1.1. Static analysis

In this problem, a simply supported square isotropic plate subjected to a uniform transverse load, q, with length, L, and thickness, h, as shown in Figure 6, is considered. The length to thickness ratios are $L/h = 10, 20, 50, 100$. For this example, the material I is used. The normalized transverse displacement is defined as:

$$\bar{w} = \left(100 E_2 h^3\right) w \left(\frac{L}{2}, \frac{L}{2}, 0\right) \Big/ \left(qL^4\right). \tag{60}$$

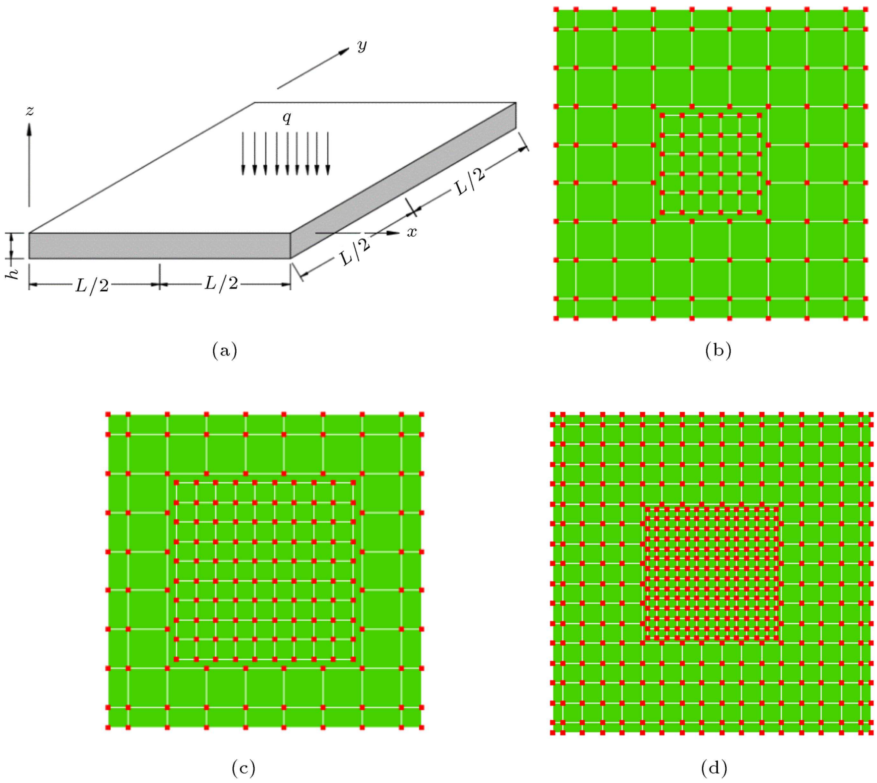

Figure 6. An isotropic plate: (a) Geometry of plate; (b), (c), and (d) control mesh based on 660, 920, and 2420 Dofs, respectively.

In order to show the capability of THB-RKPM basis functions, the convergence of normalized deflection with various L/h for quadratic and cubic elements with different control meshes, as shown in Figure 6, is studied. The present results are compared with global and local radial basis functions based on HSDT [38], FEM by Reddy [39], and the exact solution [40]. As shown in Table 1, the obtained normalized deflections with THB-RKPM method appear satisfactory. Additionally, the method presents a more accurate solution with respect to lower degrees of freedom than NURBS model does when the same order of approximation is used. Moreover, the normalized central deflections versus various L/h ratios are depicted in Figure 7. It is seen that the present results, using THB-RKPM basis functions, are close to the exact solution [40].

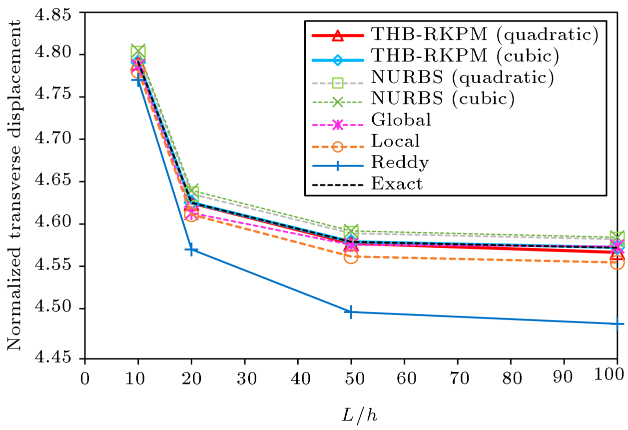

Figure 7. Central deflection of simply supported isotropic square plate with various length to thickness ratios.

4.1.2. Free vibration analysis

In order to show the applicability of THB-RKPM to modelling of the common engineering shapes in free vibration analysis, the non-dimensional frequency parameter given by $\bar{\omega} = \omega R^2 \sqrt{\rho h/D}$ for an isotropic clamped circular plate with radius R, thickness h, and flexural stiffness $D = Eh^3/12(1-\nu^2)$ is considered. The coarsest mesh of circular plate is described employing quadratic-order NURBS basis functions. The refined model with different meshes is also plotted in Figure 8. It can be seen that truncated hierarchical B-spline basis coupling with RKPM preserves the geometry when local refinement is performed. Different values of radius to thickness ratio, $R/h = 10, 100$, are considered. The results obtained by THB-RKPM are presented in Table 2 and compared with NURBS by Thai et al. [14], meshfree methods based on RKPM by Liew et al. [41], RBF by Ferreira et al. [42], and the exact solution [43]. The present computed values are in good agreement with other published data. The first

Table 1. Normalized deflection of a simply supported isotropic square plate under a uniformly distributed load.

L/h	Method	Degree	Dofs	$\bar{w}$	L/h	Method	Degree	Dofs	$\bar{w}$
10	Present	Quadratic	660	4.7895	50	Present	Quadratic	660	4.558
			920	4.7899				920	4.5696
			2420	4.7906				2420	4.5771
		Cubic	725	4.7911			Cubic	725	4.5791
			965	4.7911				965	4.579
			2525	4.7911				2525	4.579
	NURBS [14]	Quadratic	3125	4.8015		NURBS [14]	Quadratic	3125	4.5889
		Cubic	3125	4.8045			Cubic	3125	4.5919
	Global [38]	—	2205	4.7866		Global [38]	—	2205	4.5753
	Local [38]	—	2205	4.7804		Local [38]	—	2205	4.5615
	Reddy [39]	—	—	4.770		Reddy [39]	—	—	4.496
	Exact [40]	—	—	4.791		Exact [40]	—	—	4.579
20	Present	Quadratic	660	4.6211	100	Present	Quadratic	660	4.5073
			920	4.6225				920	4.5495
			2420	4.6247				2420	4.5666
		Cubic	725	4.6254			Cubic	725	4.5732
			965	4.6254				965	4.5725
			2525	4.6254				2525	4.5724
	NURBS [14]	Quadratic	3125	4.6355		NURBS [14]	Quadratic	3125	4.5819
		Cubic	3125	4.6396			Cubic	3125	4.5844
	Global [38]	—	2205	4.6132		Global [38]	—	2205	4.5737
	Local [38]	—	2205	4.6110		Local [38]	—	2205	4.5546
	Reddy [39]	—	—	4.570		Reddy [39]	—	—	4.482
	Exact [40]	—	—	4.625		Exact [40]	—	—	4.572

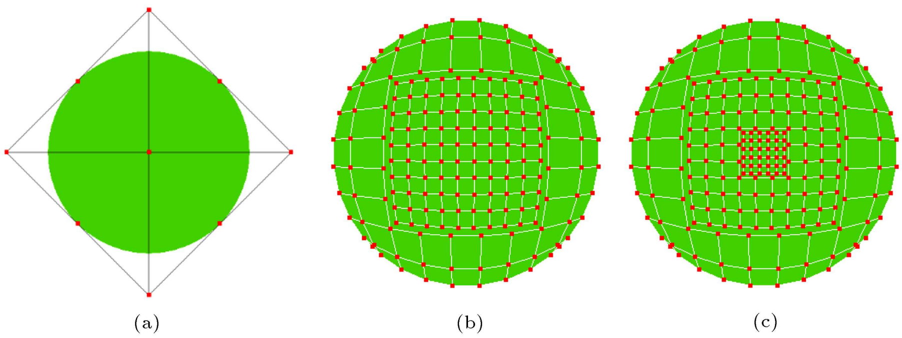

Figure 8. Circular plate: (a) Coarse mesh with one element; (b) and (c) two levels of refinement.

4 mode shapes for the circular plate with $R/h = 10$ are plotted in Figure 9.

4.1.3. Buckling analysis

Consider the simply supported rectangular isotropic plate subjected to in-plane compression loading, see Figure 10. The non-dimensional buckling load intensity factor $\bar{\lambda} = b^2\lambda_{cr}/(\pi^2 D)$ is computed using quadratic and cubic basis functions with hierarchical meshes. The critical buckling load intensity factors $\bar{\lambda}$ with respect to 3 different thickness to width ratios, $h/b = 0.05, 0.1, 0.2$, and 5 length to width ratios, $a/b = 0.5, 1, 1.5, 2, 2.5$, are tabulated in Table 3. Also, the present results are compared with NURBS basis functions, the meshfree method based on the reproducing kernel particle approximate by Liew et al. [41], and pb-2 Ritz method presented by Kitipornchai et al. [44]. It is observed that the present values by

Table 2. The first 6 frequencies of an isotropic clamped circular plate.

R/h	Method	Degree	Dofs	Modes 1	2	3	4	5	6
10	Present	Cubic	965	9.967	20.2802	32.4402	36.7952	46.3328	54.5315
		Quartic	1020	9.9641	20.27	32.4218	36.7534	46.2236	54.4123
	NURBS [14]	Cubic	1805	9.9439	20.1880	32.2318	36.5118	45.8242	53.9147
		Quartic	2000	9.9439	20.1880	32.2314	36.5111	45.8223	53.9113
	RKPM [41]	—	—	9.931	20.194	32.353	36.665	45.827	54.257
	RBF [42]	—	—	9.9442	20.1884	32.2313	36.5086	45.8353	53.9028
	Exact [43]	—	—	9.941	20.232	32.406	36.479	46.178	53.89
100	Present	Cubic	965	10.23	21.2805	35.178	39.867	52.7984	61.2180
		Quartic	1020	10.2127	21.2501	34.8713	39.7419	51.2015	60.8029
	NURBS [14]	Cubic	1805	10.2135	21.2554	34.8637	39.7967	51.1153	61.0447
		Quartic	2000	10.2130	21.2488	34.8470	39.7348	50.9706	60.7532
	RKPM [41]	—	—	10.2661	21.4488	35.2556	40.2905	51.6626	62.1455
	RBF [42]	—	—	10.2317	21.2684	34.9802	39.6223	52.1268	60.8731
	Exact [43]	—	—	10.2158	21.2600	34.8800	39.7710	51.0400	60.8200

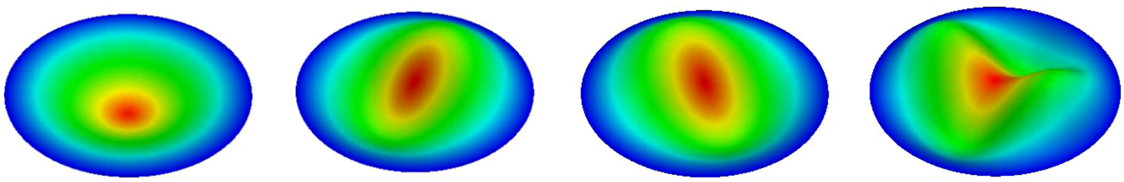
(a) (b) (c) (d)

Figure 9. The first 4 mode shapes of the clamped circular plate with $R/h = 10$.

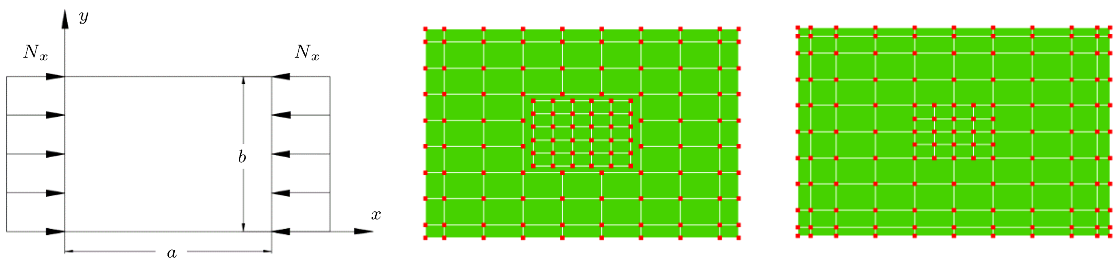

(a) (b) (c)

Figure 10. Rectangular plate with $a/b = 1.5$: (a) In-plane compression loading; (b) and (c) quadratic and cubic hierarchical meshes, respectively.

THB-RKPM are very close to the pb-2 Ritz results. From the comparisons provided in Table 3, it can be concluded that THB-RKPM basis functions with lower degrees of freedom have good performance in comparison with HSDT NURBS and FSDT meshfree methods. Furthermore, Figure 11 depicts the critical buckling load factor, $\bar{\lambda}$, against aspect ratio, a/b.

4.2. Analysis of laminated composite plates

4.2.1. Static analysis of three-layer [0/90/0] *square laminated plate under a uniformly distributed load*

Consider a laminated square plate under the simply supported boundary conditions subjected to a uniformly distributed load, q, as shown in Figure 12.

Table 3. Critical buckling load intensity factors of simply supported rectangular isotropic plates with various length to width and thickness to width ratios under uniaxial compression.

				Present		NURBS		Meshfree [41]		pb-2 Ritz [44]
			Deg.*	Quadratic	Cubic	Quadratic	Cubic	Regular particles	Irregular particles	—
			Dofs	660	725	1620	1805	867	867	—
a/b	0.5	h/b	0.05	6.0002	5.9942	5.9950	5.9942	6.0405	5.9624	6.0372
			0.1	5.3649	5.3620	5.3627	5.3620	5.3116	5.2084	5.4777
			0.2	3.8853	3.8834	3.8839	3.8834	3.7157	3.6933	3.9963
a/b	1	h/b	0.05	3.9396	3.9324	3.9331	3.9324	3.9293	3.9610	3.9444
			0.1	3.7484	3.7459	3.7463	3.7459	3.7270	3.6760	3.7865
			0.2	3.1770	3.1758	3.1760	3.1758	3.1471	3.0750	3.2637
a/b	1.5	h/b	0.05	4.2838	4.2401	4.2438	4.2404	4.2116	4.2849	4.2570
			0.1	3.9825	3.9690	3.9706	3.9690	3.8982	3.8761	4.0250
			0.2	3.2110	3.2062	3.2073	3.2062	3.1032	3.0505	3.3048
a/b	2	h/b	0.05	3.9746	3.9324	3.9367	3.9324	3.8657	4.0511	3.9444
			0.1	3.7590	3.7459	3.7474	3.7459	3.6797	3.6714	3.7865
			0.2	3.1799	3.1758	3.1766	3.1758	3.0783	3.1040	3.2637
a/b	2.5	h/b	0.05	4.1848	4.0498	4.0700	4.0498	3.9600	4.1423	4.0645
			0.1	3.8856	3.8195	3.8256	3.8195	3.7311	3.6985	3.8683
			0.2	3.1663	3.1484	3.1509	3.1484	3.0306	2.9520	3.2421

*: Degree.

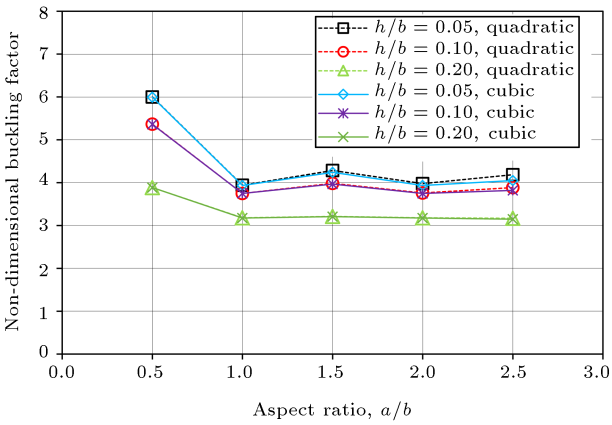

Figure 11. Critical buckling load factors of simply supported rectangular isotropic plate with various thickness to width and length to width ratios based on quadratic and cubic THB-RKPM.

The thickness to length ratios are $h/a = 0.2, 0.1, 0.05$. Material II is used in this problem. The normalized displacement of the three-layer [0/90/0] square plate is as follows:

$$\bar{w} = \left(100E_2h^3\right) w\left(\frac{a}{2}, \frac{a}{2}, 0\right) \Big/ \left(qa^4\right). \tag{61}$$

The present results are compared with those of the element-free Galerkin based on FSDT [45], the meshless local Petrov Galerkin using multiquadrics [46], exact solution [47], thin plate splines based on HSDT model [46], and 3D finite element solution [46]. The details are tabulated in Table 4. It is observed that good values of deflection are obtained by the proposed basis functions. In addition, the numerical solution obtained by THB-RKPM is computationally more efficient than other available methods, since its total number of degrees of freedom is lower than those in other methods. It should also be mentioned that EFG is based on Reissner-Mindlin plate theory with 3 degrees of freedom per each node with quadratic shape functions for transverse displacement, rotations, and 7th-order Spline for weight function.

4.2.2. Free vibration analysis of laminated composite plates

In this example, a three-layer [0°/90°/0°] elliptical plate subjected to fully clamped boundary condition

Table 4. Normalized deflection of a simply supported [0/90/0] laminated square plate under a uniformly distributed load.

h/a	Method	Degree	Dofs	$\bar{w}$
0.05	Present	Quadratic	660	0.7759
			920	0.7759
			2420	0.7758
	NURBS [14]	Quadratic	3125	0.7787
		Cubic	3125	0.7796
		Quartic	3125	0.7805
	EFG (FSDT) [45]	7th-order and quadratic	867	0.7583
	MQ-MLPG (HSDT) [46]	4th-order	3042	0.7688
	TSP-MLPG (HSDT) [46]	4th-order	3042	0.7613
	3D-FEM [46]	Quadratic	18759	0.7951
	Exact [47]	—	—	0.7572
0.1	Present	Quadratic	660	1.0898
			920	1.0898
			2420	1.0898
	NURBS [14]	Quadratic	3125	1.0937
		Cubic	3125	1.0950
		Quartic	3125	1.0963
	EFG (FSDT) [45]	7th-order and quadratic	867	1.0248
	MQ-MLPG (HSDT) [46]	4th-order	3042	1.1090
	TSP-MLPG (HSDT) [46]	4th-order	3042	1.0955
	3D-FEM [46]	Quadratic	18759	1.1401
	Exact [47]	—	—	1.0250
0.2	Present	Quadratic	660	2.1869
			920	2.1868
			2420	2.1865
	NURBS [14]	Quadratic	3125	2.1941
		Cubic	3125	2.1967
		Quartic	3125	2.1991
	MQ-MLPG (HSDT) [46]	4th-order	3042	2.1496
	TSP-MLPG (HSDT) [46]	4th-order	3042	2.1400
	3D-FEM [46]	Quadratic	18759	2.2383

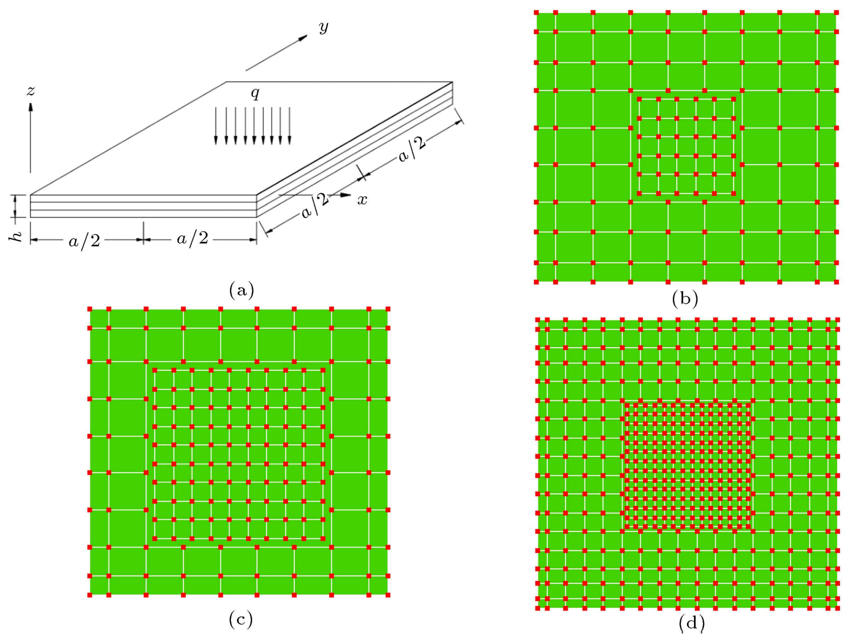

Figure 12. Square laminated plate: (a) Geometry of plate; (b), (c), and (d) control mesh based on 660, 920, and 2420 Dofs, respectively.

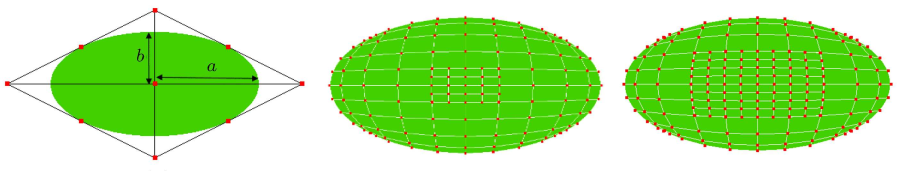

Figure 13. Elliptical plate: (a) Coarse mesh with one element; (b) and (c) two levels of refinement, respectively.

Table 5. The first 6 frequencies of a fully clamped laminated elliptical plate.

a/h	Method	Dofs	Modes					
			1	2	3	4	5	6
5	Present	725	14.4229	20.4664	27.9402	29.8436	36.1716	36.2946
		965	14.4173	20.4618	27.9338	29.8223	35.1553	36.2746
	FSDT [13]	1792	14.157	19.969	27.114	28.855	34.943	35.062
	TSDT [49]	1280	14.1353	20.0216	27.2208	28.8527	34.9609	35.2453
	SSDT [49]	1280	14.1945	20.0986	27.3172	29.0467	35.1965	35.3653
	ESDT [49]	1280	14.2711	20.1982	27.4413	29.3002	35.5012	35.519
10	Present	725	17.2846	25.9678	37.5621	39.6872	49.8718	51.4338
		965	17.2818	25.9645	37.5491	39.6753	49.8565	51.3547
	FSDT [13]	1792	17.184	25.714	36.982	39.196	49.148	50.259
	TSDT [49]	1280	17.188	25.7979	37.0987	39.0942	49.1092	50.3576
	SSDT [49]	1280	17.2128	25.8318	37.1416	39.2032	49.2466	50.4108
	ESDT [49]	1280	17.2446	25.876	37.1991	39.3431	49.4234	50.484
20	Present	725	18.3575	28.3666	42.5319	44.4824	57.3777	60.6944
		965	18.3563	28.3605	42.4719	44.4756	57.3496	60.3244
	FSDT [13]	1792	18.329	28.28	42.255	44.321	57.09	59.827
	TSDT [49]	1280	18.3666	28.4097	42.4237	44.2872	57.1596	59.9436
	SSDT [49]	1280	18.3742	28.4203	42.4372	44.3262	57.2112	59.9602
	ESDT [49]	1280	18.3837	28.4342	42.4557	44.3758	57.2773	59.9845
100	Present	725	18.7666	29.4437	45.6415	46.6351	61.5257	66.278
		965	18.7552	29.3371	44.755	46.509	60.9096	65.2853
	FSDT [13]	1792	18.755	29.332	44.792	46.508	60.792	65.6230
	TSDT [49]	1280	18.8085	29.4663	44.8105	46.5297	60.9055	64.763
	SSDT [49]	1280	18.8088	29.4667	44.8111	46.5316	60.908	64.7637
	ESDT [49]	1280	18.8092	29.4673	44.8119	46.5339	60.9112	64.7648
	EFG [48]	201	18.8100	29.5800	44.9900	46.7200	61.3400	65.1400

using Material IV is studied. The elliptical plate has two radii $a = 5$ and $b = 2.5$, as shown in Figure 13. The non-dimensional frequencies are defined by $\bar{\omega} = (\omega a^2)\left(\sqrt{\rho h/D_0}\right)$ with $D_0 = E_1 h^3/12(1-\nu_{12}\nu_{21})$. Table 5 presents the normalized first 6 frequencies of the laminated clamped elliptical plate with various radius to thickness ratios. Since there is no analytical solution, the results obtained are compared with those of the isogeometric analysis using layerwise first-order shear deformation theory (LW-FSDT) [13], the element free Galerkin method based on Classical Laminate Plate Theory (CLPT) [48], and layerwise higher-order shear deformation theory via NURBS based isogeometric analysis using different shape functions [49]. For the thick plate, the solution obtained is slightly larger than those of other methods. The first 6 mode shapes of a three-layer fully clamped laminated elliptical plate with $a/h = 20$ are depicted in Figure 14.

As the last example in this section, a laminated composite square plate with a hole of very complicated shape is analyzed to demonstrate applicability of the present method to the analysis of laminated plates with complicated shapes. Material IV is used and geometrical parameters are shown in Figure 15 with thickness $h = 0.06$ and length $a = 10$. The natural frequency is normalized by $\bar{\omega} = \left(\frac{\omega^2 a^4 \rho h}{D_0}\right)^{\frac{1}{2}}$. As shown

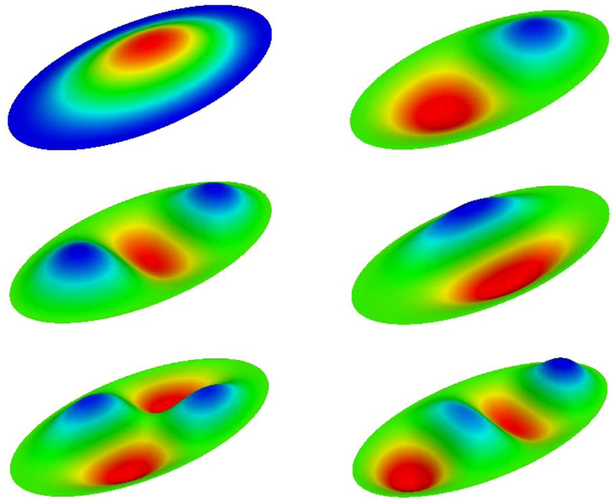

Figure 14. Six mode shapes of an elliptical three-layer [0/90/0] clamped laminated plate with $a/h = 20$.

in Figure 15(b), the plate is divided into 8 patches and the bending strip method [50] is employed to maintain C^1-continuity between patches. Quadratic THB-RKPM basis functions with 432 control points are applied to this problem. Table 6 presents the first 6 normalized frequencies of the three-ply laminated plate with simply supported boundary conditions and various fiber orientations. The THB-RKPM solutions are compared with the results obtained by the Element-Free Galerkin (EFG) and Moving Kriging Interpolation (MKI) methods [25]. It is observed that the results obtained by quadratic truncated hierarchical B-splines coupling with RKPM are in good agreement with EFG and MKI methods for all the considered orientations.

4.2.3. Buckling analysis of laminated composite plates

A four-layer cross-ply [0/90/90/0] laminate square plate subjected to uniaxial compression with simply supported boundaries is analyzed to investigate the convergence of the present method for the buckling problems. The critical buckling load is non-dimensionalized as follows:

$$\bar{\lambda} = a^2 \lambda_{cr}/(E_2 h^3), \tag{62}$$

where a and h are the edge length and thickness of the composite plate. Material III is used in this section. The convergence of the normalized critical buckling load with different numbers of degrees of freedom and various modulus ratios is presented in Table 7. The numerical results obtained are compared with those of the research by Noor and Mathers [51] based on the 3D elasticity solution, isogeometric analysis by Thai et al. [14], the meshfree radial basis function method by Liu et al. [52], finite element solution based on HSDT by Phan and Reddy [53], and finite element method by Khdeir and Librescu [54]. It is observed that the proposed formulation presents good performance. It is also seen that by increasing the E_1/E_2 modulus ratio, the normalized critical buckling load increases.

Next, in order to assess the effect of the length to thickness ratio a/h on the uniaxial compression load intensity, two- and four-layer simply supported cross-ply square plates are considered. The critical buckling loads of two- and four-layer simply supported plates are presented in Table 8. It can be seen that the present method has acceptable results and the critical buckling loads become larger with increase in span to thickness ratio. Finally, a three-layer cross-ply [0/90/0] simply supported square plate under bi-axial buckling load, as shown in Figure 16, with length a and thickness h is considered. The effect of modulus ratio E_1/E_2 with $a/h = 10$ on the critical bi-axial buckling load is studied in this example. Table 9 shows the normalized critical buckling loads with respect to various modulus ratios. It is observed that by increasing the modulus ratio E_1/E_2, the normalized critical bi-axial buckling load

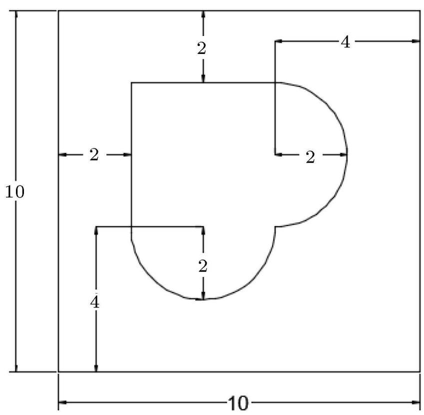

(a)

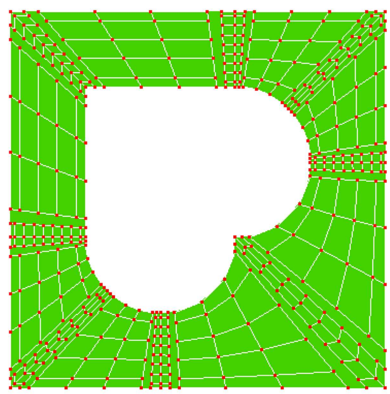

(b)

Figure 15. A laminated composite square plate with a hole of complicated shape: (a) Geometrical parameters and (b) control mesh with 432 control points.

Table 6. The normalized natural frequencies of simply supported three-ply laminate plate with a complicated hole for various orientations.

Angle ply	**Method**	**Modes**					
		1	**2**	**3**	**4**	**5**	**6**
$[0°/0°/0°]$	Present	18.233	31.098	35.648	55.387	62.334	81.897
	NURBS [55]	18.288	31.110	35.735	55.499	62.464	82.033
	EFG [25]	18.226	31.127	36.237	56.874	62.390	83.565
	MKI [25]	18.169	30.303	36.581	57.429	64.145	85.656
$[15°/-15°/15°]$	Present	18.965	32.195	36.024	56.211	63.564	83.679
	NURBS [55]	19.020	32.260	36.078	56.480	63.727	83.830
	EFG [25]	19.177	32.445	37.238	58.716	63.994	86.500
	MKI [25]	18.323	31.472	37.617	63.077	66.538	86.486
$[30°/-30°/30°]$	Present	20.379	34.056	36.988	58.434	66.195	88.071
	NURBS [55]	20.448	34.184	37.179	58.660	66.310	88.107
	EFG [25]	20.926	34.915	39.101	62.222	67.054	92.715
	MKI [25]	20.310	33.987	39.898	58.111	69.699	92.099
$[45°/-45°/45°]$	Present	21.011	34.896	37.463	59.459	67.743	91.041
	NURBS [55]	21.128	35.122	37.692	59.545	67.948	91.196
	EFG [25]	21.736	36.079	39.975	63.897	68.525	96.767
	MKI [25]	20.987	34.897	39.269	63.375	69.017	96.588
$[0°/90°/0°]$	Present	18.134	31.129	35.532	55.481	62.652	82.554
	NURBS [55]	18.284	31.267	35.713	55.567	62.892	82.631
	EFG [25]	18.278	32.264	36.134	57.151	65.853	90.678
	MKI [25]	18.027	32.506	37.268	57.698	70.768	92.998

Table 7. Normalized critical buckling load of simply supported cross-ply [0/90/90/0] square plate with $a/h = 10$ and various E_1/E_2 ratios.

a/h	**Method**	**Degree**	**Dofs**	E_1/E_2				
				3	**10**	**20**	**30**	**40**
10	Present	Quadratic	220	5.3591	9.8699	15.2014	19.5679	23.2330
		Cubic	250	5.3186	9.8203	15.1416	19.4991	23.1558
	NURBS [14]	Quadratic	1805	5.3876	9.9195	15.2459	19.5852	23.2126
		Cubic	2000	5.3867	9.9174	15.2427	19.5814	23.2082
	Noor and Mathers [51]	Cubic	315	5.294	9.762	15.019	19.304	22.881
	Phan and Reddy [53]	Cubic	567	5.114	9.774	15.298	19.957	23.340
	Liu et al. [52]	—	2000	5.412	10.013	15.309	19.778	23.412
	Khdeir and Librescu [54]	—	—	5.442	10.026	15.019	19.304	22.881

Table 8. Convergence of normalized critical buckling loads of cross-ply simply supported square plates.

Layer	Method	Degree	Dofs	a/h 10	20	50	100
[0°/90°]	Present	Quadratic	220	11.4174	12.6993	13.5509	14.3216
		Cubic	250	11.3258	12.4982	12.8904	12.9727
	NURBS [14]	Quadratic	1805	11.5360	12.5794	12.9043	12.9584
		Cubic	2000	11.5315	12.5741	12.8977	12.9472
	FSDT [56]	Quadratic	7623	11.349	12.510	12.879	12.934
	MISQ24 [57]	Quadratic	1734	11.446	12.609	13.011	13.095
	FSDT [58]	—	—	11.353	12.515	12.884	12.939
	HSDT [58]	—	—	11.563	12.577	12.895	12.942
[0°/90°/90°/0°]	Present	Quadratic	220	23.2330	31.7510	36.1106	37.9609
		Cubic	250	23.1558	31.5584	35.3343	35.9830
	NURBS [14]	Quadratic	1805	23.2126	31.6407	35.3607	35.9771
		Cubic	2000	23.2082	31.6325	35.3497	35.9612
	FSDT [56]	Quadratic	7623	23.409	31.625	35.254	35.851
	MISQ24 [57]	Quadratic	1734	23.236	31.747	35.561	36.190
	FSDT [58]	—	—	23.471	31.707	35.356	35.955
	HSDT [58]	—	—	23.349	31.637	35.419	35.971

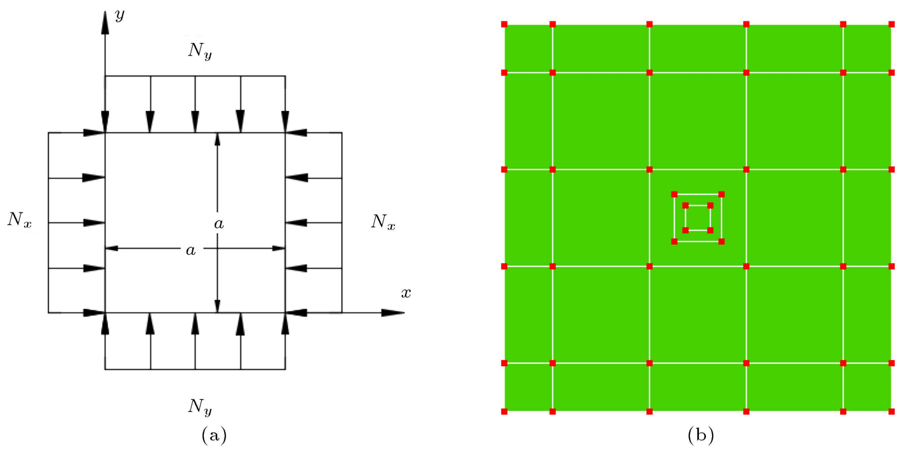

Figure 16. A three-layer cross-ply [0/90/0] simply supported square plate: (a) Geometry of the composite plate under bi-axial compression, and (b) control mesh based on 220 Dofs.

also increases. Once again, the present results show good agreement with other numerical results cited here.

5. Conclusions

In this paper, our main focus was on local refinement of laminated plates. Therefore, the truncated hierarchical B-splines were coupled with the reproducing kernel meshfree shape functions to investigate static, buckling, and free vibration of multilayered plates. Since a correspondence between meshfree methods and isogeometric analysis was established, the nodes and their related meshfree shape functions were constructed in a meshfree environment, which led to geometry exactness and model refinement. The main novelty of the proposed method was introducing a flexible coupling strategy for refining basis functions to decrease the computational cost without losing accuracy of the solution. In the proposed approach, after defining the linear reproducing points, basis functions were constructed through a one-step process and more importantly, after generating new meshfree nodes, recomputing the shape functions based on the new node group was omitted because the original basis functions were truncated to produce the new basis ones. This means that, instead of calculating all basis functions,

Table 9. Bi-axial critical buckling load of a three-layer [0/90/0] simply supported cross-ply square plate.

a/h	Method	Degree	Dofs	E_1/E_2			
				10	20	30	40
10	Present	Quadratic	220	4.8807	7.3956	8.9131	10.0615
		Cubic	250	4.8561	7.3302	8.6372	9.7834
	NURBS [14]	Quadratic	1805	4.9777	7.5446	8.9429	10.1096
		Cubic	2000	4.9766	7.5429	8.9383	10.1046
	MISQ24 [57]	Quadratic	1734	4.939	7.488	9.016	10.252
	HSDT [54]	—	—	4.963	7.516	9.056	10.259
	FSDT [59]	—	—	4.963	7.588	8.575	10.202

only a number of bases were modified, which improved the computational performance and considerably facilitated the adaptive local refinement. It also caused the computing cost to be lower than those of the existing methods. The advantage of preserving the exact geometry throughout the refinement process was also inherited. Displacement, frequencies, and critical buckling loads were computed using quadratic and cubic orders of THB-RKPM basis functions. The results of the present method proved its high accuracy for all test cases with various geometrical shapes, boundary conditions, and aspect ratios. Hence, this method can be applied to practical problems of engineering with integrated advanced materials.

References

1. Dimitri, R., Fantuzzi, N., Li, Y., and Tornabene, F. "Numerical computation of the crack development and SIF in composite materials with XFEM and SFEM", *Composite Structures*, **160**, pp. 468-490 (2017).

2. Liu, B., Huang, L., Kaveendran, B., Geng, L., Cui, X., Wei, S., and Yin, F. "Tensile and bending behaviors and characteristics of laminated Ti-(TiBw/Ti) composites with different interface status", *Composites Part B: Engineering*, **108**, pp. 377-385 (2017).

3. Monti, A., El Mahi, A., Jendli, Z., and Guillaumat, L. "Experimental and finite elements analysis of the vibration behaviour of a bio-based composite sandwich beam", *Composites Part B: Engineering*, **110**, pp. 466-475 (2017).

4. Jari, H., Atri, H., and Shojaee, S. "Nonlinear thermal analysis of functionally graded material plates using a NURBS based isogeometric approach", *Composite Structures*, **119**, pp. 333-345 (2015).

5. Behjat, B., Salehi, M., Armin, A., Sadighi, M., and Abbasi, M. "Static and dynamic analysis of functionally graded piezoelectric plates under mechanical and electrical loading", *Scientia Iranica*, **18**, pp. 986-994 (2011).

6. Alashti, R.A., Khorsand, M., and Tarahhomi, M. "Thermo-elastic analysis of a functionally graded spherical shell with piezoelectric layers by differential quadrature method", *Scientia Iranica*, **20**, pp. 109-119 (2013).

7. Carrera, E., Brischetto, S., and Nali, P., *Plates and Shells for Smart Structures: Classical and Advanced Theories for Modeling and Analysis*, John Wiley & Sons (2011).

8. Carrera, E., Cinefra, M., and Li, G. "Refined finite element solutions for anisotropic laminated plates", *Composite Structures*, **183**, pp. 63-76 (2018).

9. Reddy, J.N., *Mechanics of Laminated Composite Plates and Shells: Theory and Analysis*, CRC press (2004).

10. Hughes, T.J., Cottrell, J.A., and Bazilevs, Y. "Isogeometric analysis: CAD, finite elements, NURBS, exact geometry and mesh refinement", *Computer Methods in Applied Mechanics and Engineering*, **194**, pp. 4135-4195 (2005).

11. Guo, Y. and Ruess, M. "A layerwise isogeometric approach for NURBS-derived laminate composite shells", *Composite Structures*, **124**, pp. 300-309 (2015).

12. Natarajan, S., Ferreira, A., and Nguyen-Xuan, H. "Analysis of cross-ply laminated plates using isogeometric analysis and unified formulation", *Curved Layer. Struct.*, **1**, pp. 1-10 (2014).

13. Thai, C.H., Ferreira, A., Carrera, E., and Nguyen-Xuan, H. "Isogeometric analysis of laminated composite and sandwich plates using a layerwise deformation theory", *Composite Structures*, **104**, pp. 196-214 (2013).

14. Thai, C.H., Nguyen-Xuan, H., Bordas, S.P.A., Nguyen-Thanh, N., and Rabczuk, T. "Isogeometric analysis of laminated composite plates using the higher-order shear deformation theory", *Mechanics of Advanced Materials and Structures*, **22**, pp. 451-469 (2015).

15. Sederberg, T.W., Cardon, D.L., Finnigan, G.T., North, N.S., Zheng, J., and Lyche, T. "T-spline simplification and local refinement", *ACM Transactions on Graphics (TOG)*, **23**, pp. 276-283 (2004).

16. Forsey, D.R. and Bartels, R.H. "Hierarchical B-spline refinement", *ACM Siggraph Computer Graphics*, **22**, pp. 205-212 (1988).

17. Li, X., Deng, J., and Chen, F. "Surface modeling with polynomial splines over hierarchical T-meshes", *The Visual Computer*, **23**, pp. 1027-1033 (2007).
18. Dokken, T., Lyche, T., and Pettersen, K.F. "Polynomial splines over locally refined box-partitions", *Computer Aided Geometric Design*, **30**, pp. 331-356 (2013).
19. Giannelli, C., Jüttler, B., Kleiss, S.K., Mantzaflaris, A., Simeon, B., and Špeh, J. "THB-splines: An effective mathematical technology for adaptive refinement in geometric design and isogeometric analysis", *Computer Methods in Applied Mechanics and Engineering*, **299**, pp. 337-365 (2016).
20. Li, X., Zheng, J., Sederberg, T.W., Hughes, T.J., and Scott, M.A. "On linear independence of T-spline blending functions", *Computer Aided Geometric Design*, **29**, pp. 63-76 (2012).
21. Scott, M., Li, X., Sederberg, T., and Hughes, T. "Local refinement of analysis-suitable T-splines", *Computer Methods in Applied Mechanics and Engineering*, **213**, pp. 206-222 (2012).
22. Bressan, A. and Jüttler, B. "A hierarchical construction of LR meshes in 2D", *Computer Aided Geometric Design*, **37**, pp. 9-24 (2015).
23. Johannessen, K.A., Kvamsdal, T., and Dokken, T. "Isogeometric analysis using LR B-splines", *Computer Methods in Applied Mechanics and Engineering*, **269**, pp. 471-514 (2014).
24. Kraft, R., *Adaptive and Linearly Independent Multilevel B-Splines*, SFB 404, Geschäftsstelle (1997).
25. Bui, T.Q., Nguyen, M.N., and Zhang, C. "An efficient meshfree method for vibration analysis of laminated composite plates", *Computational Mechanics*, **48**, pp. 175-193 (2011).
26. Somireddy, M. and Rajagopal, A. "Meshless natural neighbor Galerkin method for the bending and vibration analysis of composite plates", *Composite Structures*, **111**, pp. 138-146 (2014).
27. Rosolen, A. and Arroyo, M. "Blending isogeometric analysis and local maximum entropy meshfree approximants", *Computer Methods in Applied Mechanics and Engineering*, **264**, pp. 95-107 (2013).
28. Valizadeh, N., Bazilevs, Y., Chen, J., and Rabczuk, T. "A coupled IGA-Meshfree discretization of arbitrary order of accuracy and without global geometry parameterization", *Computer Methods in Applied Mechanics and Engineering*, **293**, pp. 20-37 (2015).
29. Sambridge, M., Braun, J., and Mcqueen, H. "Geophysical parametrization and interpolation of irregular data using natural neighbours", *Geophysical Journal International*, **122**, pp. 837-857 (1995).
30. González, D., Cueto, E., and Doblaré, M. "Higher-order natural element methods: Towards an isogeometric meshless method", *International Journal for Numerical Methods in Engineering*, **74**, pp. 1928-1954 (2008).
31. Zhang, H. and Wang, D. "Reproducing kernel formulation of B-spline and NURBS basis functions: A meshfree local refinement strategy for isogeometric analysis", *Computer Methods in Applied Mechanics and Engineering*, **320**, pp. 474-508 (2017).
32. Chi, S.-W. and Lin, S.-P. "Meshfree analysis with the aid of NURBS boundary", *Computational Mechanics*, **58**, pp. 371-389 (2016).
33. Atri, H. and Shojaee, S. "Meshfree truncated hierarchical refinement for isogeometric analysis", *Computational Mechanics*, **62**, pp. 1583-1597 (2018).
34. Piegl, L. and Tiller, W., *The NURBS Book*, Springer Science & Business Media (2012).
35. Faraji, S., Kolahdoozan, M., and Afshar, M. "Collocated Mixed Discrete Least Squares Meshless (CMDLSM) method for solving quadratic partial differential equations", *Scientia Iranica*, **25**, pp. 2000-2011 (2018).
36. Reddy, J.N. "A simple higher-order theory for laminated composite plates", *Journal of Applied Mechanics*, **51**, pp. 745-752 (1984).
37. Faraji, S., Kolahdoozan, M., and Afshar, M. "Mixed discrete least squares meshless method for solving the linear and non-linear propagation problems", *Scientia Iranica*, **25**, pp. 565-578 (2018).
38. Roque, C., Cunha, D., Shu, C., and Ferreira, A. "A local radial basis functions-finite differences technique for the analysis of composite plates", *Engineering Analysis with Boundary Elements*, **35**, pp. 363-374 (2011).
39. Reddy, J.N., *An Introduction to the Finite Element Method*, McGraw-Hill, New York (1993).
40. Reddy, J., *Energy and Variational Methods in Applied Mechanics, 1984*, Springer Science, and Business Media (2000).
41. Liew, K., Wang, J., Ng, T., and Tan, M. "Free vibration and buckling analyses of shear-deformable plates based on FSDT meshfree method", *Journal of Sound and Vibration*, **276**, pp. 997-1017 (2004).
42. Ferreira, A., Roque, C., Neves, A., Jorge, R., Soares, C., and Liew, K.M. "Buckling and vibration analysis of isotropic and laminated plates by radial basis functions", *Composites Part B: Engineering*, **42**, pp. 592-606 (2011).
43. Liew, K.-M., Xiang, Y., Kitipornchai, S., and Wang, C., *Vibration of Mindlin Plates: Programming the p-version Ritz Method*, Elsevier (1998).
44. Kitipornchai, S., Xiang, Y., Wang, C., and Liew, K. "Buckling of thick skew plates", *International Journal for Numerical Methods in Engineering*, **36**, pp. 1299-1310 (1993).
45. Belinha, J. and Dinis, L. "Analysis of plates and laminates using the element-free Galerkin method", *Computers & Structures*, **84**, pp. 1547-1559 (2006).

46. Xiao, J., Gilhooley, D., Batra, R., Gillespie, J., and Mccarthy, M. "Analysis of thick composite laminates using a higher-order shear and normal deformable plate theory (HOSNDPT) and a meshless method", *Composites Part B: Engineering*, **39**, pp. 414-427 (2008).

47. Reddy, J.N., *Mechanics of Laminated Composite Plates: Theory and Analysis*, CRC press (1997).

48. Chen, X., Liu, G., and Lim, S. "An element free Galerkin method for the free vibration analysis of composite laminates of complicated shape", *Composite Structures*, **59**, pp. 279-289 (2003).

49. Thai, C.H., Ferreira, A., Wahab, M.A., and Nguyen-Xuan, H. "A generalized layerwise higher-order shear deformation theory for laminated composite and sandwich plates based on isogeometric analysis", *Acta Mechanica*, **227**, pp. 1225-1250 (2016).

50. Kiendl, J., Bazilevs, Y., Hsu, M.-C., Wüchner, R., and Bletzinger, K.-U. "The bending strip method for isogeometric analysis of Kirchhoff—Love shell structures comprised of multiple patches", *Computer Methods in Applied Mechanics and Engineering*, **199**, pp. 2403-2416 (2010).

51. Noor, A.K. and Mathers, M.D., *Shear-Flexible Finite-Element Models of Laminated Composite Plates and Shells*, National Aeronautics and Space Administration Hampton Va Langley Research Center (1975).

52. Liu, L., Chua, L., and Ghista, D. "Mesh-free radial basis function method for static, free vibration and buckling analysis of shear deformable composite laminates", *Composite Structures*, **78**, pp. 58-69 (2007).

53. Phan, N. and Reddy, J. "Analysis of laminated composite plates using a higher-order shear deformation theory", *International Journal for Numerical Methods in Engineering*, **21**, pp. 2201-2219 (1985).

54. Khdeir, A. and Librescu, L. "Analysis of symmetric cross-ply laminated elastic plates using a higher-order theory: Part II-Buckling and free vibration", *Composite Structures*, **9**, pp. 259-277 (1988).

55. Shojaee, S., Valizadeh, N., Izadpanah, E., Bui, T., and Vu, T.-V. "Free vibration and buckling analysis of laminated composite plates using the NURBS-based isogeometric finite element method", *Composite Structures*, **94**, pp. 1677-1693 (2012).

56. Chakrabarti, A. and Sheikh, A. "Buckling of laminated composite plates by a new element based on higher order shear deformation theory", *Mechanics of Advanced Materials and Structures*, **10**, pp. 303-317 (2003).

57. Nguyen-Van, H., Mai-Duy, N., Karunasena, W., and Tran-Cong, T. "Buckling and vibration analysis of laminated composite plate/shell structures via a smoothed quadrilateral flat shell element with in-plane rotations", *Computers & Structures*, **89**, pp. 612-625 (2011).

58. Reddy, J. and Phan, N. "Stability and vibration of isotropic, orthotropic and laminated plates according to a higher-order shear deformation theory", *Journal of Sound and Vibration*, **98**, pp. 157-170 (1985).

59. Fares, M. and Zenkour, A. "Buckling and free vibration of non-homogeneous composite cross-ply laminated plates with various plate theories", *Composite Structures*, **44**, pp. 279-287 (1999).

Biographies

Hamid Reza Atri obtained his BS and MS degrees from Shahid Bahonar University of Kerman, Iran. He is currently a PhD candidate in the College of Civil Engineering at Shahid Bahonar University of Kerman. His research interests are mainly concentrated on isogeometric and finite element analysis.

Saeed Shojaee obtained his BS degree from Shahid Bahonar University of Kerman in 2001 and his MS and PhD degrees in Structural Engineering from Iran University of Science and Technology in 2003 and 2007, respectively. He is currently Associate Professor in the Department of Civil Engineering at Shahid Bahonar University in Kerman, Iran. His main interests include computational mechanics, optimal analysis and design of structures, and metaheuristic optimization techniques and applications.